The Astronomical Journal, 159:94 (17pp), 2020 March https://doi.org/10.3847/1538-3881/ab665b
© 2020. The American Astronomical Society. All rights reserved.

Kepler-1661 b: A Neptune-sized *Kepler* Transiting Circumbinary Planet around a Grazing Eclipsing Binary

Quentin J Socia[1], William F Welsh[1], Jerome A Orosz[1], William D Cochran[2], Michael Endl[2], Billy Quarles[3], Donald R Short[1], Guillermo Torres[4], Gur Windmiller[1], and Mitchell Yenawine[1]
[1] Department of Astronomy, San Diego State University, 5500 Campanile Drive, San Diego, CA 92182-1221, USA
[2] McDonald Observatory, The University of Texas as Austin, Austin, TX 78712-0259, USA
[3] Center for Relativistic Astrophysics, School of Physics, Georgia Institute of Technology, Atlanta, GA 30332, USA
[4] Center for Astrophysics | Harvard & Smithsonian, 60 Garden Street, Cambridge, MA 02138, USA
Received 2019 August 13; revised 2019 December 18; accepted 2019 December 18; published 2020 February 10

Abstract

We report the discovery of a Neptune-sized ($R_p = 3.87 \pm 0.06 R_\oplus$) transiting circumbinary planet, Kepler-1661 b, found in the *Kepler* photometry. The planet has a period of ∼175 days and its orbit precesses with a period of only 35 yr. The precession causes the alignment of the orbital planes to vary, and the planet is in a transiting configuration only ∼7% of the time as seen from Earth. As with several other *Kepler* circumbinary planets, Kepler-1661 b orbits close to the stability radius, and is near the (hot) edge of the habitable zone. The planet orbits a single-lined, grazing eclipsing binary, containing a $0.84\,M_\odot$ and $0.26\,M_\odot$ pair of stars in a mildly eccentric ($e = 0.11$), 28.2 day orbit. The system is fairly young, with an estimated age of ∼1–3 Gyr, and exhibits significant starspot modulations. The grazing eclipse configuration means the system is very sensitive to changes in the binary inclination, which manifests itself as a change in the eclipse depth. The starspots contaminate the eclipse photometry, but not in the usual way of inducing spurious eclipse timing variations. Rather, the starspots alter the normalization of the light curve, and hence the eclipse depths. This can lead to spurious eclipse depth variations, which are then incorrectly ascribed to binary orbital precession.

Unified Astronomy Thesaurus concepts: Eclipsing binary stars (444); Exoplanet astronomy (486); Exoplanet detection methods (489); Timing variation methods (1703); Transit photometry (1709)

1. Introduction

If an exoplanet orbits two stars instead of one, it complicates the detection, characterization, and long-term behavior of the system. Yet, it also provides the opportunity to measure the stellar and planetary properties with exquisite precision. If the host stars are eclipsing and are bright enough for both their radial velocities to be measured, then we can directly determine the stellar masses, radii, temperatures, and age using the traditional binary star analysis techniques. If in addition the exoplanet transits the stars, then much more information about the binary system is available: the transit times tell us about the relative locations of the bodies, and the transit durations tell us about the relative velocities. The transit depths provide further information about the precession of the orbits and place much tighter constraints on the limb darkening and system parameters. It is no surprise that the circumbinary planet (CBP) systems have among the most accurate and precisely known stellar and planet parameters, e.g., the masses and radii of the stars in Kepler-34 are known to better than 0.3%, and the planet's radius to 1.7% (Welsh et al. 2012); in Kepler-16, the planet's radius is known to an astonishing 0.35% (Doyle et al. 2011). Even when the secondary star's radial velocity is not measurable, the full set of system parameters can still be determined. The transits provide the information necessary to determine the binary mass ratio, something impossible in a classical single-lined eclipsing binary system.[5] See the review by Welsh & Orosz (2018) for more on this topic.

However, such richness comes with a cost. The orbital motion of the planet is decidedly non-Keplerian, so the equations of motion need to be numerically integrated, including corrections for general relativity and apsidal motion. More importantly, the standard technique for exoplanet mass determination—measurement of the Doppler reflex motion of the host star—has not yet worked for a CBP. The meters-per-second radial velocity induced by the planet is completely dwarfed by the much shorter timescale and larger amplitude velocity variation caused by the companion star. Fortunately, there is a way to determine the planet's mass: the planet induces variations in the eclipse times. The larger the planet's mass, the larger the eclipse timing variations (ETVs). The orbital period, eccentricity, and argument of periastron can be measured, and the planet need not be transiting to be detected: the orbital inclination can be constrained given high-enough quality data. See Borkovits et al. (2011, 2015) for a full discussion of the ETV method. Note that eclipses are usually much deeper than transits, and therefore the eclipse times can be measured with very high precision, even with ground-based photometry. An eclipse timing uncertainty of 10 s in a 30 day binary amounts to a precision of 4 ppm. So even though the planet barely perturbs the binary, at this precision its presence can be felt. Unlike radial velocities, ETVs due to precession grow with time, so a long temporal baseline can more than compensate for less-than-*Kepler*-quality observations.

KIC 6504534 was discovered and cataloged as a ∼28.2 day eclipsing binary system in the second revision of the *Kepler* Eclipsing Binary Catalog[6] (Prša et al. 2011; Slawson et al. 2011). At the time the binary was discovered, the planet was

[5] We use the term "eclipse" to refer to mutual star-star crossings, and the term "transit" for a planet crossing in front of a star. No occultations are seen in Kepler-1661.

[6] http://keplerebs.villanova.edu/

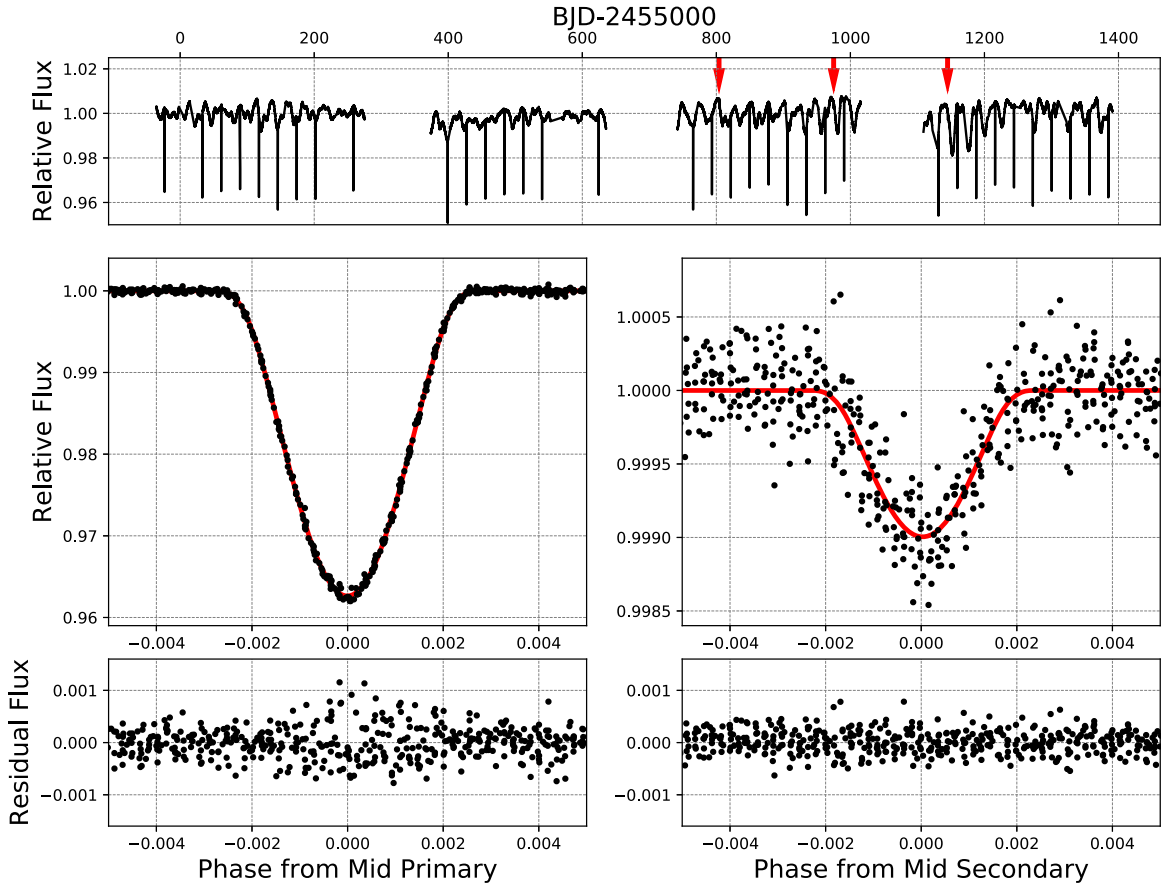

Figure 1. The normalized *Kepler* light curve of Kepler-1661 is shown in the upper panel with the abscissa representing BJD–2,455,000. Each Quarter was detrended with a cubic polynomial. The red arrows indicate where the three transits of the planet occur. The lower panels show the orbital phase–folded primary and secondary eclipses, along with an initial model fit and residuals. The V-shaped primary eclipse immediately tells us that the eclipse is grazing. The residuals show a larger scatter during eclipse than outside eclipse, most likely due to changes in the normalized eclipse depth caused by starspots.

not transiting. The first transit (near BJD 2455804.8, 2011 August 11 UT) did not occur until Quarter 10. Visual inspection of the light curve revealed a second transit near BJD 2455975.1 (2012 February 17) in the Quarter 12 data, allowing a rough estimate of 180 days to be made for the candidate's orbital period. The target was requested to be observed in Short Cadence mode (approximately 2 minute sampling instead of 30 minutes) and the planet candidate was given the designation KOI-3152. A third transit was observed in Quarter 14 (BJD 2456145.5, 2012 August 5), but sadly a fourth transit event that occurred in Quarter 16 fell in a gap and was not observed.

KOI-3152, now known as Kepler-1661, is a single-lined eclipsing binary, so the mass ratio cannot be determined from the radial velocities alone. While in principle transits can provide enough information to determine the mass ratio (e.g., this was done for Kepler-16; Doyle et al. 2011), the three transits in Kepler-1661 all occur near the same binary orbital phase (phase 0.40, 0.45, 0.5) and thus provide only limited information on the primary star's orbit. This fundamentally limits our ability to precisely measure the system parameters. Nevertheless, there is enough information to fully characterize the binary, and photodynamical modeling clearly establishes the candidate as a CBP. In Section 2 we present the observations, and in Section 3 review the photodynamical modeling at length, with particular emphasis on treatment of the effects of starspots in the light curve. In Section 4 we discuss the results and properties of the binary star and new CBP, and present our conclusions in Section 5.

2. Observations

2.1. Kepler *Data*

All available data on Kepler-1661 were retrieved from MAST in early 2019, corresponding to *Kepler* Data Release DR25. We use the SAP (Simple Aperture Photometry) calibration, not the PDC-MAP calibration, because we find it preserves intrinsic stellar variability with higher fidelity. Kepler-1661 fell on one of the failed CCD modules (module 3) and thus no observations are available for Quarters 5, 9, 13, and 17. This results in three ∼90 day gaps in the light curve which otherwise is superb, as is typical of *Kepler* photometry. Quarters 14, 15, and 16 have Short Cadence data available, and these were used in the preliminary investigation and for building a template eclipse profile for the eclipse timing measurements. However, because of the relative faintness of the target, these were not used in the final photodynamical modeling. The upper panel of Figure 1 shows the entire *Kepler* light curve. For this figure, each Quarter was detrended and normalized using a third order polynomial. The primary eclipses are readily seen, as are ripples due to starspots. A total of 36 primary eclipses are present, although two are missing ingress data and are mostly unusable. The primary eclipses have a fractional depth of ∼0.038; in contrast, the 36

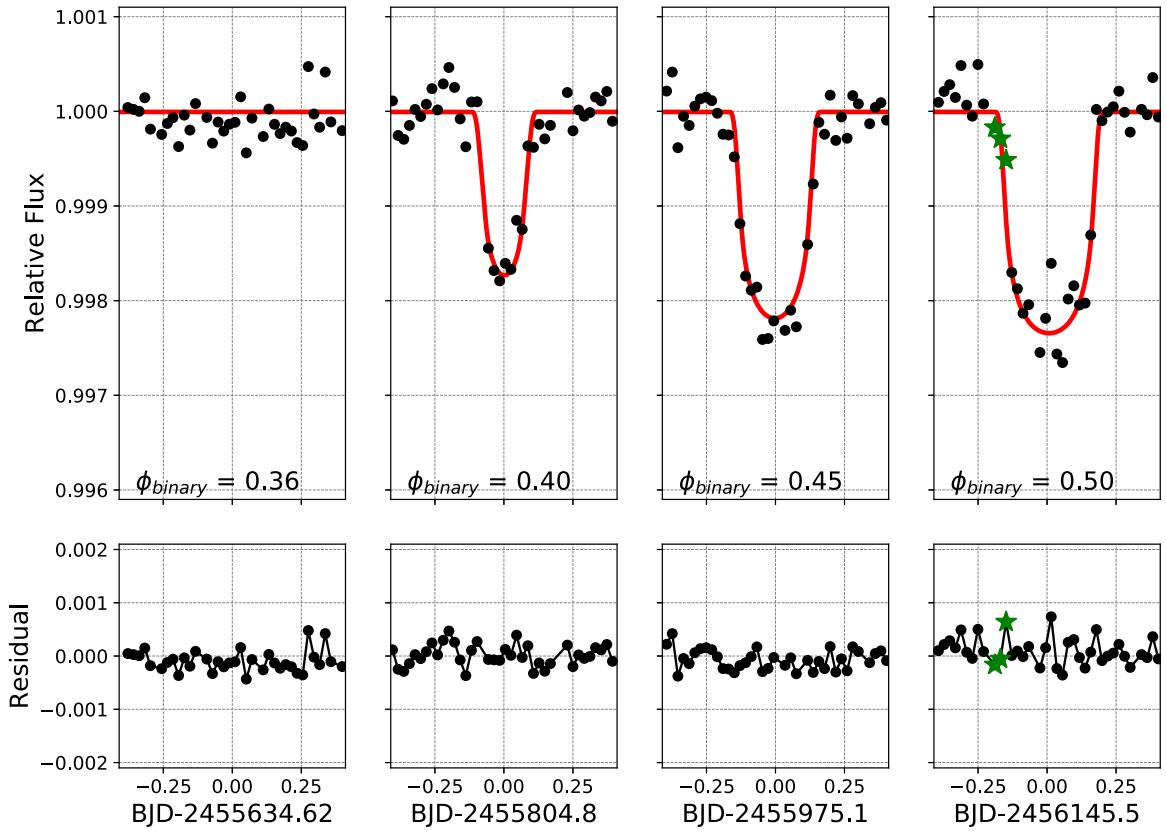

Figure 2. Upper panels: transits of the planet across the primary star, and the best-fit model. The changing depths and widths are a classic signature of a circumbinary object. In general, the depth and width changes are due to the varying relative position and velocities of the star and planet at the times of transit. However for Kepler-1661, the orbital phase of the binary during the transits are similar, so the changes in the transit profiles are mainly due to the changing impact parameter caused by the precession of the planet's orbit. The orbital phase of the binary star is given in the upper panels. The first panel shows no transit, though this is where one would expect a transit to occur if the planet's orbit did not precess so much that the absolute value of the impact parameter is greater than one. The three green "star" points in the rightmost panel lie near a rejected observation, and they have had their uncertainties boosted by a factor of 10. Lower panels: residuals (data minus model) of the fits.

secondary eclipses are not even visible on this scale, having a fractional depth of only ∼0.001. Also shown in Figure 1 are the phase-folded eclipse profiles. Before folding on the orbital period, each eclipse was detrended and normalized by masking out the eclipse and fitting a third order polynomial to a narrow window surrounding each eclipse, and the data were then divided by the polynomial fit. The shallow depths and V-shaped eclipses are indicative of grazing eclipses. The residuals of an initial model fit to the eclipses are flat for the secondary, but show an increased scatter during the primary eclipse. This indicates a change in eclipse depth, potentially due to starpots.

Also present in the light curve are three transits, and notably, the transit depths increase from ∼0.0018 to 0.0023 as shown in Figure 2. This change in transit depth implies a change in the inclination (or impact parameter) of the planet's orbit, a consequence of rapid precession. The transit widths also increase, consistent with a decrease in the impact parameter, though a change in transit duration can also be caused by a change in the relative velocity of the planet and star at different orbital phases of the star. During the third transit ingress there is a datum missing, and the *Kepler* pipeline Data Quality flag indicates a cosmic ray hit occurred on the CCD column at this time. The ingress looks by eye to be fine, but to be cautious, we boosted the uncertainty on the data points after this cosmic ray event by a factor of 10.

The *Kepler* Input Catalog (KIC) provides the following estimates for the stellar parameters: Kepmag = 14.216, $T_{\rm eff}$ = 4748 K, $\log g$ = 4.46, metallicity = −0.10, and a contamination = 0.00 for all four *Kepler* Seasons. In general, the KIC estimates should be used with considerable caution for binary stars, but in this case the primary star dominates the light from the system (see Section 4.1) so these estimates should not be heavily biased.

2.2. Mt. Laguna Observatory Photometry

A primary eclipse on 2019 June 3 (UT) was observed in the Johnson–Cousins *R*-band with the Mount Laguna Observatory (MLO) 1 m telescope. Exposures of 120 s were used and the CCD pixels were binned 2 × 2 during readout, giving an effective pixel size of 0.″8, more than adequate for the relatively poor 3″ average seeing that night. Standard data calibration was performed using AstroImageJ (AIJ; Collins et al. 2017), and differential photometry carried out using six comparison stars within 3′ of the target. AIJ utilizes the UTC2BJD calculator (Eastman et al. 2010) to convert UT to BJD times.

The time interval from the first to the last primary eclipse in the *Kepler* light curve was 1407 days. The eclipse provided by MLO more than doubles the temporal baseline, extending it to 3660 days (10 yr). Figure 3 shows the MLO light curve. A mideclipse time of 2458637.8570 ± 0.0003 BJD was measured, which is within 1σ of the extrapolated linear ephemeris determined from the *Kepler* primary eclipses. It should be noted that due to the different bandpass, and hence limb

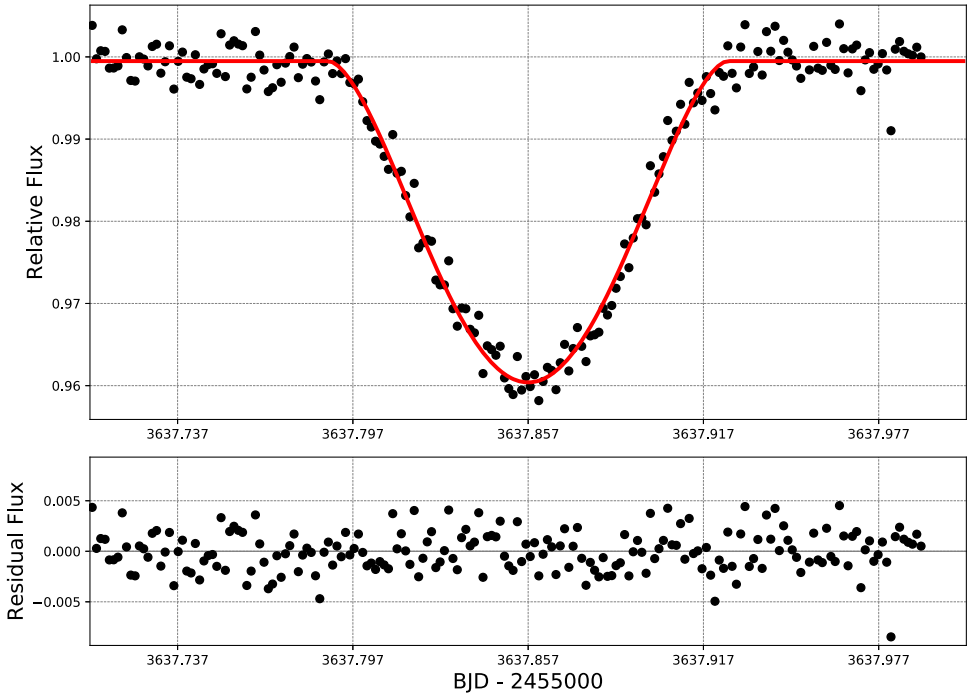

Figure 3. Normalized and detrended MLO *R*-band primary eclipse with the best-fit photodynamical model shown in red. The eclipse depth is slightly deeper than the *Kepler* eclipses because of the wavelength-dependence of the limb darkening combined with the high impact parameter of the grazing eclipse.

darkening, the *R*-band eclipse shape and depth are different from that seen by *Kepler*.

2.3. Spectroscopy and Radial Velocities

We obtained high-resolution spectra with three instruments: the HRS spectrograph on the Hobby–Eberly Telescope (HET; Tull 1998), the Tull Coude spectrograph on the 2.7 m Smith telescope at McDonald Observatory (Tull et al. 1995), and the echelle spectrograph on the 4 m Mayall telescope at Kitt Peak National Observatory (KPNO). The radial velocity standard star HD 182488 was observed with each spectrograph to assist in calibration of the velocity zero-point. The HET and 2.7 m Smith telescope observations used Coude spectrographs and made targeted observations of Kepler-1661. The Mayall telescope observations used a Cassegrain spectrograph and the observations were made as part of a survey of *Kepler* eclipsing binaries. The former observations have higher accuracy than the latter.

A total of 11 radial velocities were obtained over the course of 2012 and 2013, and are listed in Table 1. Only the primary star's spectrum was detectable in the spectra, consistent with the very shallow secondary eclipses. The radial velocity curve is shown in Figure 4 and is well matched by our photodynamical model fit (discussed in Section 3.4) with a radial velocity semiamplitude (K) of 17.3 km s^{-1} and eccentricity 0.11. Nearly identical values are obtained when just the radial velocities alone are fit with a simple binary star model.

Using the Kea code (Endl & Cochran 2016) on the 2.7 m observations (these have the highest spectral resolution, $R \sim$ 60,000) yields a mean effective temperature of 5140 ± 50 K, metallicity [M/H] = −0.12 ± 0.10 dex, $\log(g) = 4.66 \pm 0.10$ cgs, and $V_{\rm rot} \sin i = 2.5 \pm 0.5$ km s^{-1}.

For an independent estimate of the temperature, we used published photometry to compute five color indices, dereddened using four different dust maps (giving $E(B-V) = 0.056$ for an assumed distance of 400 pc). The Casagrande et al. (2010) color/temperature transformations yield an average $T_{\rm eff}$ of 5070 ± 110 K, assuming solar metallicity and that the secondary star does not contribute a significant amount of light. This is in excellent agreement with the spectroscopic value. As a final value, we adopt an effective temperature for the primary star of 5100 ± 100 K.

Table 1
Kepler-1661 Radial Velocity Measurements

Date (BJD)	RV (km s^{-1})	σ (km s^{-1})	Instrument
2456017.921467	17.42	0.07	HET
2456022.921967	−0.46	0.04	HET
2456039.871467	30.20	0.06	HET
2456138.837280	−3.34	0.05	HET
2456230.586181	10.44	0.06	HET
2456083.794858	−2.59	0.15	KPNO
2456086.841888	4.96	0.15	KPNO
2456088.949298	10.42	0.16	KPNO
2456091.888598	19.25	0.20	KPNO
2456138.759680	−3.40	0.16	Tull
2456238.605381	31.34	0.18	Tull

2.4. Gaia *Parallax*

Gaia Mission data for Kepler-1661 (*Gaia* DR2 2104078025612319360) were retrieved from the *Gaia* Data Release 2 (Gaia Collaboration et al. 2016, 2018). *Gaia* measured a parallax of 2.407 ± 0.017 mas, giving a distance of 415 ± 3 parsecs. With this distance, plus the precise absolute *Gaia* photometry and the effective temperature, we can estimate the radius of the primary star, assuming the secondary star contributes a negligible amount of light. This assumption is consistent with the lack of detection of the secondary in the spectroscopy and the shallow eclipse depth in the photometry.

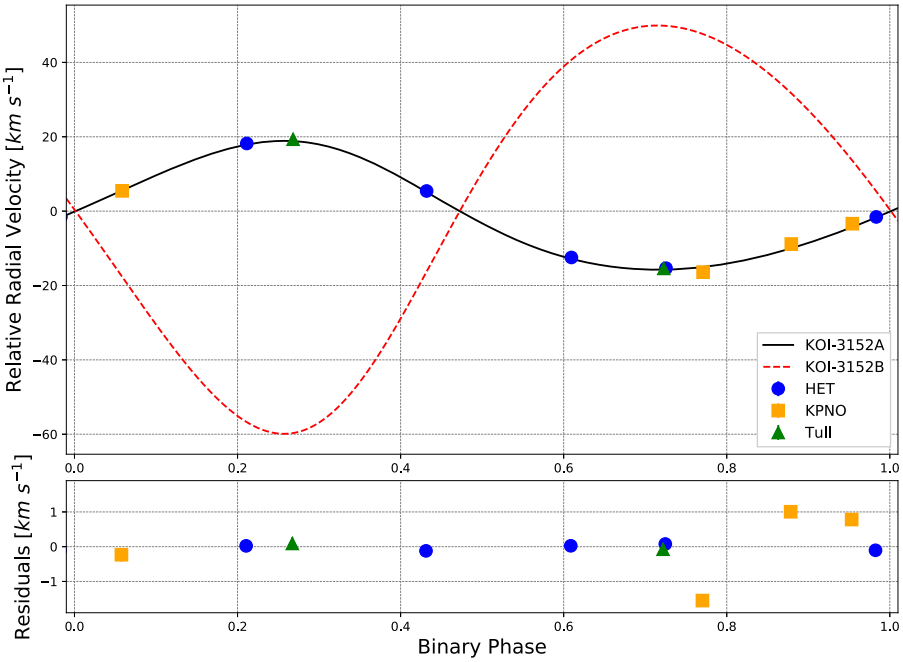

Figure 4. Radial velocities of the primary star with the best model fit folded on the binary period. The uncertainties in the velocities are smaller than the symbols. The secondary star is not detected in the spectra, but its expected radial velocity curve is shown as the red dashed curve.

It is later shown to be completely justified by the photodynamical model.

We used the conversion given by the *Gaia* Collaboration to estimate the bolometric correction to the *G*-band magnitude of 14.19 (with an estimated error of 0.02 mag) and an extinction of $E(B-V) = 0.056 \pm 0.02$. We derive a radius of $0.743 \pm 0.042\,R_{\odot}$ for the primary star. The uncertainty in the temperature is the dominant source of the uncertainty, but the uncertainty in the reddening is a major contributor.

2.5. Photometric Contamination

With 4″ pixels and an aperture several pixels across, the potential for unwanted light to be included in the *Kepler* photometry is significant. Since this extra light has the effect of reducing the eclipse and transit depths, and thus the stellar and planetary radii (and other correlated parameters), it is important to constrain the excess light contamination as much as possible. The MAST website gives a contamination level of zero for all Quarters, except Quarter 1 which has a contamination of 0.0004 listed.

To verify this, we queried the *Gaia* catalog for any objects within 40″ of Kepler-1661 and found that of the 15 objects returned, only one was sufficiently close and bright enough to possibly contaminate the *Kepler* photometry: *Gaia* DR2 2104078025609950464, which is KIC 6504533. Located ∼9″ away, it is 6.55 mag dimmer in the *Gaia G* bandpass (Riello et al. 2018) and if this star were *entirely* within the *Kepler* aperture it would account for only ∼0.003 of the observed flux. But in fact this star does not lie within the *Kepler* aperture for any Quarter.

Aligning and stacking together our MLO *R*-band data into one image (∼7 hr exposure), we confirm the nearby star's location and brightness. This star is well outside of the aperture used to generate the MLO light curve, and we found no other sources of light near Kepler-1661. Finally, we examined the *Kepler* Target Pixel Files and found no indication of additional background light, nor any image centroid movement during eclipse. Thus the very low level of contamination listed at MAST seems correct and we treat the contamination as negligible for all Quarters.

3. Photodynamical Modeling

3.1. The ELC Photodynamical Model

We performed a simultaneous fit of all the eclipses and transits along with the radial velocity measurements using the eclipsing light curve code "ELC" (Orosz & Hauschildt 2000; Wittenmyer et al. 2005; Orosz et al. 2019). The code integrates the equations of motion using Newtonian gravity with general relativistic corrections (Hilditch 2001; Mardling & Lin 2002; Ragozzine & Wolf 2009). A "tidal" term is also included to account for the nonspherical potentials, which leads to classical apsidal motion, but this effect is negligible in comparison to the dynamical and general relativistic precession (which themselves are small). A twelfth order Gaussian Runge–Kutta symplectic integrator is used, based on the code of Hairer & Hairer (2003).[7] We employed both a nested sampling algorithm (Skilling 2004) and a Differential Evolution Monte Carlo Markov Chain (DE-MCMC) technique to sample the posterior distribution of the parameters (ter Braak & Vrugt 2006) and estimate their uncertainties.

The model stellar eclipses and planet transits are computed using the method outlined in Short et al. (2018), replacing the Mandel & Agol (2002) and Giménez methods (Giménez 2006) formerly used in ELC. A quadratic limb darkening law is used, following the prescription of Kipping (2013) to more efficiently sample the correlated limb darkening coefficients. A total of 25 parameters are used in the model: the 5 standard Keplerian orbital parameters for each orbit (P, T_c, i, e, ω), the masses and radii of the three bodies, the stellar temperatures, 2 quadratic limb darkening coefficients for each star in the *Kepler* and *R*-

[7] The code can be downloaded at http://www.unige.ch/math/folks/hairer.

bandpasses, and the longitudinal nodal angle Ω_p of the planet's orbit (Ω_b of the binary is set fixed to zero). In the actual fitting procedure, ratios and other combinations of parameters are often better constrained by the data or better sampled by the DE-MCMC process and therefore these equivalent parameters are used, e.g., orbital velocity of the primary K_1, mass ratios, radius ratios, temperature ratio, $\sqrt{e}\cos\omega$, and $\sqrt{e}\sin\omega$. The temperature of the primary star is also a free parameter though the light curves and radial velocity observations cannot constrain it. The spectroscopically determined value and its uncertainty are included as a datum that the model needs to match (i.e., it is included in the χ^2 statistic). The same procedure is used to steer the solutions toward the primary star radius determined with the *Gaia* parallax. The radius is free to be any value but there is a penalty should it deviate from the *Gaia*-derived prior.

3.2. Initial Model Fits

Although the model produced a generally acceptable match to the observations, the initial runs of ELC did not yield satisfactory results in two ways. First, the best-fit primary star mass climbed as high as the model allowed ($\sim 2\,M_\odot$). This is inconsistent with the spectroscopically determined temperature, photometric colors, and distance (see Section 2). Based on the observed stellar temperature, metallicity, and radius from the *Gaia* parallax (and their uncertainties), and matching these with the Dartmouth stellar model isochrones (Dotter et al. 2008), we estimated that the mass of the primary star should be in the range 0.71–0.88 $M_\odot$. As a single-lined binary, the mass ratio is derived from the constraints placed by the three transits, not the radial velocity of the secondary star. The transits perhaps provide only a very weak constraint on the mass ratio, and so a highly uncertain primary mass is found. But to strongly favor such a high mass with small uncertainty is implausible.

The second disconcerting initial result was the estimated high mass of the planet. The planet's radius is well determined by the light curve and the geometric and orbital constraints, and was found to be $\sim 3.6\,R_\oplus$. It was therefore extremely unlikely that the $\sim 140\,M_\oplus$ mass that the models favored was accurate. For comparison, the empirical mass–radius relations from Lissauer et al. (2011) and Weiss & Marcy (2014) give $\sim$9–15 $M_\oplus$. A low-mass planet is also favored by the lack of variations seen in the eclipse timing $O-C$ diagram (see Section 4.2.1).

Looking closely at the residuals of the primary eclipse fits provided some insight (the secondary eclipses are very noisy and are all well matched within their large uncertainties). There was correlated noise in the residuals, which we initially thought was due to the secondary star crossing a starspot on the primary star, as such occultations do result in large residuals and skew the mideclipse time (e.g., see Kepler-47, Orosz et al. 2012, 2019, and Kepler-453, Welsh et al. 2015). However two lines of reasoning lead us to reject this hypothesis. First, the narrow eclipse profiles indicate that the eclipses are grazing, and this is confirmed by the initial model: the impact parameter was close 1.0. (In fact greater than 1.0 if the impact parameter is defined by the stellar radius only, not the sum of the radii.) The other line of reasoning comes from the lack of correlation between the eclipse timing variations and the local slope of the light curve. Modulations in the light curve are due to starspots moving across the star's disk, and eclipses that cover the starspot skew the eclipse shape creating a deviation in the apparent mideclipse time (Mazeh et al. 2015). Such a correlation is seen on other circumbinary hosts, e.g., Kepler-47, -453, and -1647 (Kostov et al. 2016). Though not impossible, it is unlikely that starspots reside so near the pole of the primary star assuming the star behaves like the Sun. The lack of any correlation, despite Kepler-1661 certainly having starspots, supports the notion that starspots are not being eclipsed. Although no starspot crossing events were found, looking more closely at the eclipse residuals revealed an interesting pattern: the model eclipses were in general too deep at early times and too shallow toward the end of the *Kepler* data. This could be the result of a change in the inclination of the binary caused by precession of its orbit. This in turn would favor a high-mass planet. This seems somewhat plausible, given that we observe the rapid precession of the planet (the transits grow significantly deeper over a span of less than a year). However, as described in the next section, we believe the primary eclipse depth change to be somewhat spurious, not a real consequence of a changing impact parameter.

3.3. Eclipse Depth Variations: Cause and Effect

The eclipses and transits are *relative* changes in the observed brightness of the system: the *Kepler* data that are modeled with ELC are normalized and detrended such that the out-of-eclipse flux is 1.0. For most cases this is fine, but for Kepler-1661 the eclipse depths are shallow and very sensitive to a change in impact parameter—or an incorrect normalization that can occur if starspots are present.

The usual method to "flatten" the light curve outside of eclipses can introduce a bias in the eclipse depth if starspots are present. This is easy to visualize: suppose an eclipse of an immaculate star is 10% deep. Now suppose a starspot blocks 50% of the star's light. The 10% deep eclipse will now appear to be 20% deep in the normalized light curve. In Kepler-1661, the modulations that starspots create in the light curve are not only significant, but they are variable. It is this variability that is particularly troublesome. This changing starspot amplitude can induce an apparent change in the normalized eclipse depth. Although the starspot amplitudes are somewhat stochastic, there is a mild general trend toward larger amplitudes in the second half of the light curve, as shown in Figure 5 along with the measured primary eclipse depths. This then has the effect of an overall increase in apparent eclipse depth. The measured eclipse depth variations, while very small ($\sim$2000 ppm), are a nonnegligible fraction of the eclipses: $\sim$1% rms of the eclipse depth with a maximum change of $\sim$5%. The photodynamical model attempts to fit this changing depth by changing the inclination via a precession in the orbit of the binary.

The mass of a CBP has traditionally been determined by the ETVs. The ETVs manifest themselves as the divergence of the primary and secondary eclipse times in an $O-C$ diagram, and also the "ripples" at the planet's orbital timescale that are superimposed on the long-term apsidal divergence. However, a third observable signature is present: the eclipse depth variations. To illustrate its effect, in Figure 6 we show model primary eclipse light curves in the *Kepler* bandpass that span the observations in this study. All parameters are identical to the best-fit solution presented in Section 3.4, with the exception of the planet mass. Four cases are examined, with the planet mass set to 17, 170, 850, and 1700 $M_\oplus$. At the start of the *Kepler* data the eclipses are identical in depth and width. Toward the end of the *Kepler* data the depths are still similar (though still measurable at *Kepler* precision in the hundreds of ppm), however a significant ETV can be seen for the larger

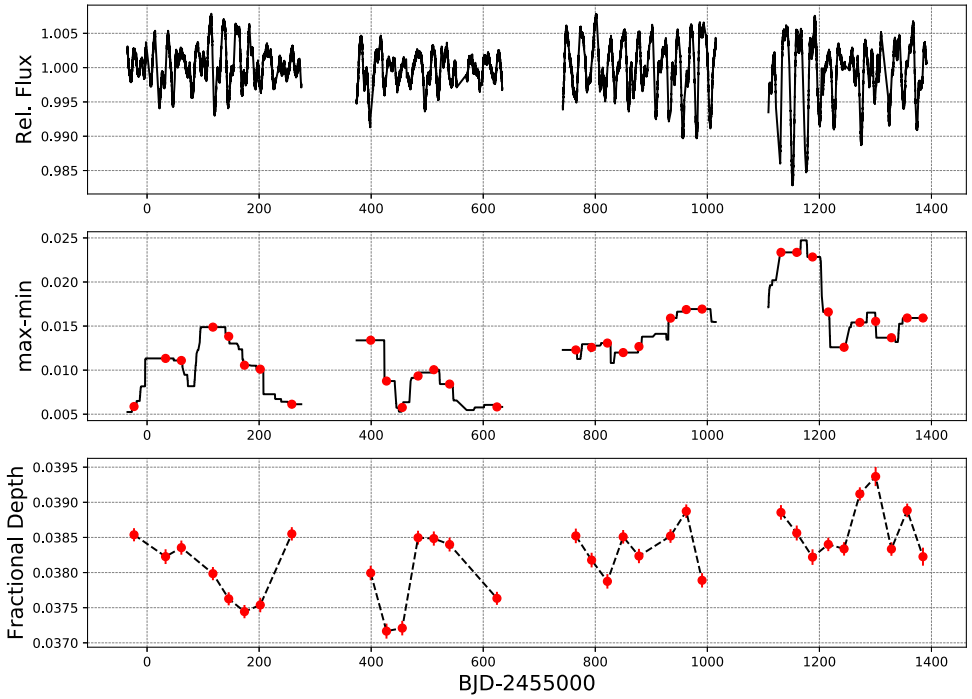

Figure 5. Upper panel: the normalized *Kepler* light curve sans eclipses, highlighting the starspot modulations. Middle panel: the peak-to-peak amplitude of the starspot modulation over a 50 day wide sliding window. The red dots mark the locations of observed primary eclipses. Bottom panel: the measured primary eclipse depths. Note the slight overall upward trend over the course of the observations, indicating an increase in eclipse depth.

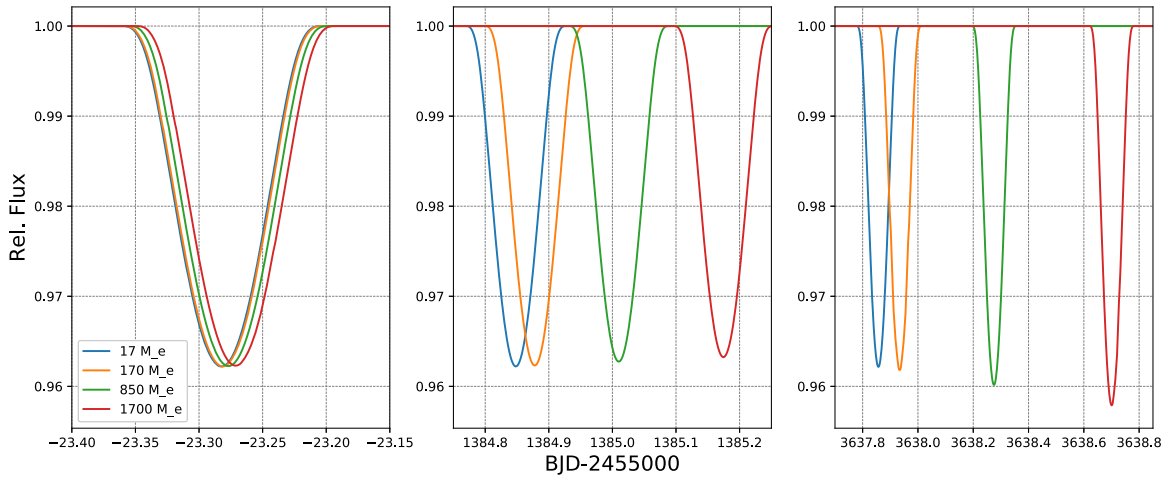

Figure 6. Four different model primary eclipse profiles in the *Kepler* bandpass are shown, spanning the duration of the observations. The best-fit 17 $M_\oplus$ model is shown in blue. The other cases use identical parameters except for the planet mass: 170 $M_\oplus$ in orange, 850 $M_\oplus$ in green, and 1700 $M_\oplus$ in red. In the middle panel the eclipse timing variations are easily seen as the shift of the eclipses from the nominal case. In the right-hand panel, the eclipse depth variations are now also easily noticeable. There is also a more subtle change in eclipse width, although it is less pronounced than the depth variation.

planet masses. The mass of the planet simultaneously affects the eclipse timing, depth, and duration making them highly correlated. Pushing out to the epoch of the Mt. Laguna Observatory observation in 2019, the change in eclipse depth becomes readily apparent. The change in depth is ∼29 ppm for a 17 $M_\oplus$ planet, ∼400 ppm for a 170 $M_\oplus$ planet, ∼2000 ppm for a 850 $M_\oplus$ planet, and ∼4400 ppm for a 1700 $M_\oplus$ (=5.35 $M_{\rm Jup}$) planet. The point of this exercise is that eclipse depth variations depend on the planet's mass, and inverting this, the planet's mass can be constrained by the observed depth variations. However, this is true only if the depth variations are real changes in inclination of the binary, not created or biased by starspots; else, a spurious planet mass may be inferred. We believe this is the cause of the failure of our initial modeling. See Appendix for information on attempting to debias the eclipse depths.

3.4. Revised Modeling and Results

3.4.1. The Final Data Set and Isochrone Constraint

Since the apparent eclipse depths vary depending on the presence of starspots, and the model is very sensitive to depth changes because of the grazing eclipse geometric configuration, we employed a technique that worked well for another CBP, Kepler-453 (Welsh et al. 2015). In that system, starspot modulations with a peak-to-peak variation of up to 1.5% are present, and residuals of the fits to the eclipses clearly showed

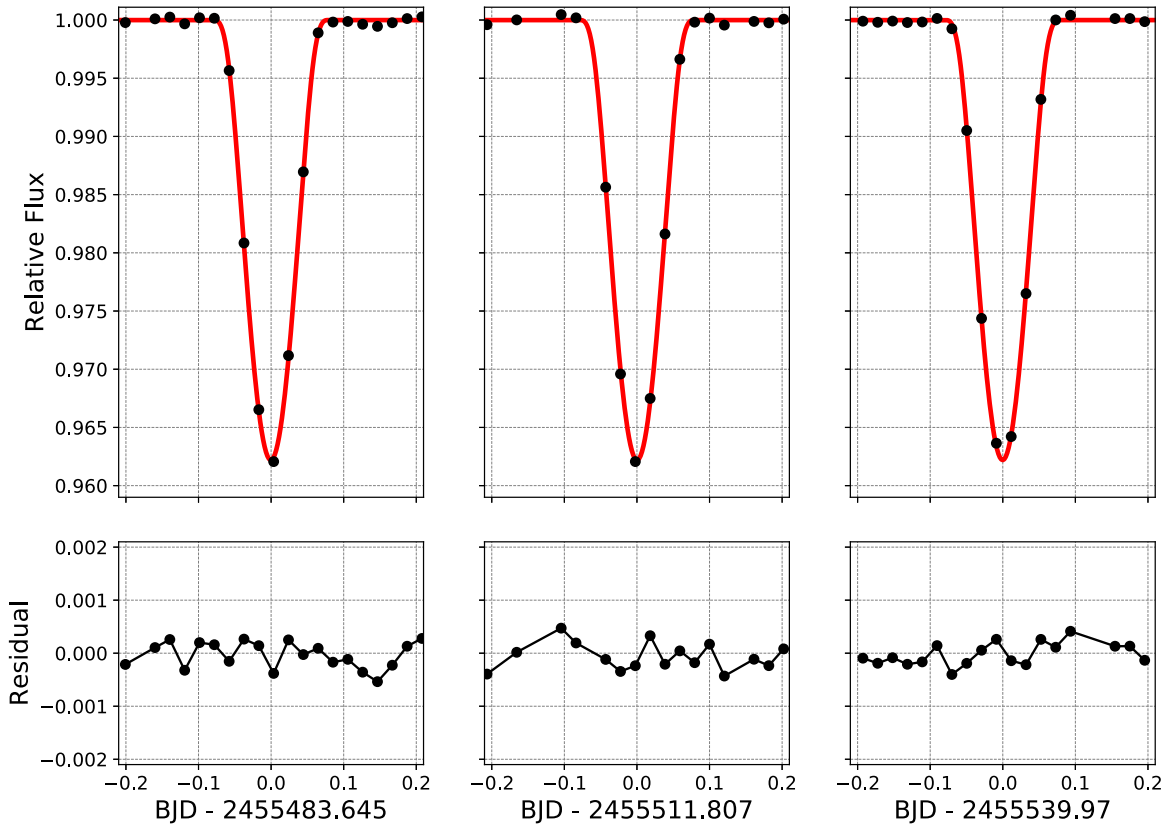

Figure 7. The three primary eclipses that are fit with our photodynamical model. The grazing eclipses create sharp, V-shaped eclipse profiles that are well matched by the model (shown in red).

that the secondary star was sometimes eclipsing starspots on the primary star. These starspot-eclipse events skew the shape of the eclipse, resulting in an erroneous planet mass. (It is the ETVs that constrain the mass of the planet, and skewed eclipses produce spurious timing variations.) To mitigate the contamination caused by starspot eclipses in Kepler-453, only three clean primary eclipses were used. For the rest of the eclipses, only their eclipse times were used. Three eclipses were enough to the characterize the binary, and the eclipse times were statistically corrected for the starspot crossing bias by measuring, then removing, the correlation with the local light curve slope. For Kepler-1661, we employed the same technique, with one minor difference: no correlation of the ETVs and local slope was seen, and so no correction was applied. The three eclipses that were fit were selected at times when the starspot activity was low.

Thus the final data set includes the 3 observed transits, 11 radial velocities, the Mt. Laguna primary eclipse, 3 *Kepler* primary eclipses, all observed *Kepler* secondary eclipses, 34 mideclipse times for the primary and 36 for the secondary, 2 windows of the *Kepler* light curve at times when transits *would* have occurred if the planet's impact parameter were not changing, and finally, 1 light curve window where a transit over the secondary could have occurred. In addition there are 2 additional data values, the temperature and primary radius measurements, for a grand total of 3457 data points. See Figure 7 for the three primary eclipses used and Figure 8 for the closest secondary eclipses.

Because this is a single-lined spectroscopic binary and the planet transits do not constrain the mass ratio tightly enough to ensure a physically plausible stellar mass solution, we incorporate an additional feature into the ELC photodynamical model: a isochrone constraint. At each iteration, the trial solution's primary star mass and radius are compared to the PARSEC stellar isochrones (Bressan et al. 2012) that span ages from 1 to 10 Gyr for a metallicity of −0.10. If for a given mass the radius is not within the range bracketed by the isochrones, then a penalty is incurred. The penalty is treated as an addition to the χ^2 value, and is computed as the square of the deviation of the radius from the 1 or 10 Gyr isochrone boundary, divided by 0.5% of the radius value, i.e., $(R - R_{\rm boundary})/0.005R)^2$. This is akin to assuming a half-percent error bar on the radius. The effect of this new feature is to steer the photodynamical solutions into a plausible region in the mass–radius plane.

3.4.2. The System Parameters

The ELC photodynamical model and the nested sampling and DE-MCMC techniques were able to satisfactorily fit the "three eclipses plus eclipse times" data set. In particular, the mass of the primary star ($0.84 \pm 0.02\,M_\odot$) and of the planet ($17 \pm 12\,M_\oplus$) are very reasonable values. The best-fit χ^2 is 4396 for 3457 degrees of freedom, or a reduced χ^2_ν of 1.27. The DE-MCMC posteriors were generally Gaussian shaped with well-determined standard deviations. The exception to this were the limb darkening parameters. Our best-fit solution (lowest χ^2) is presented in Table 2 for the parameters fit by ELC. Table 3 lists the system parameters, and Table 4 gives the instantaneous velocities and positions of the three bodies at the reference epoch. The values allow an exact numerical integration and reproduction of our model, noting that the orbits are non-Keplerian and evolve rapidly with time. The

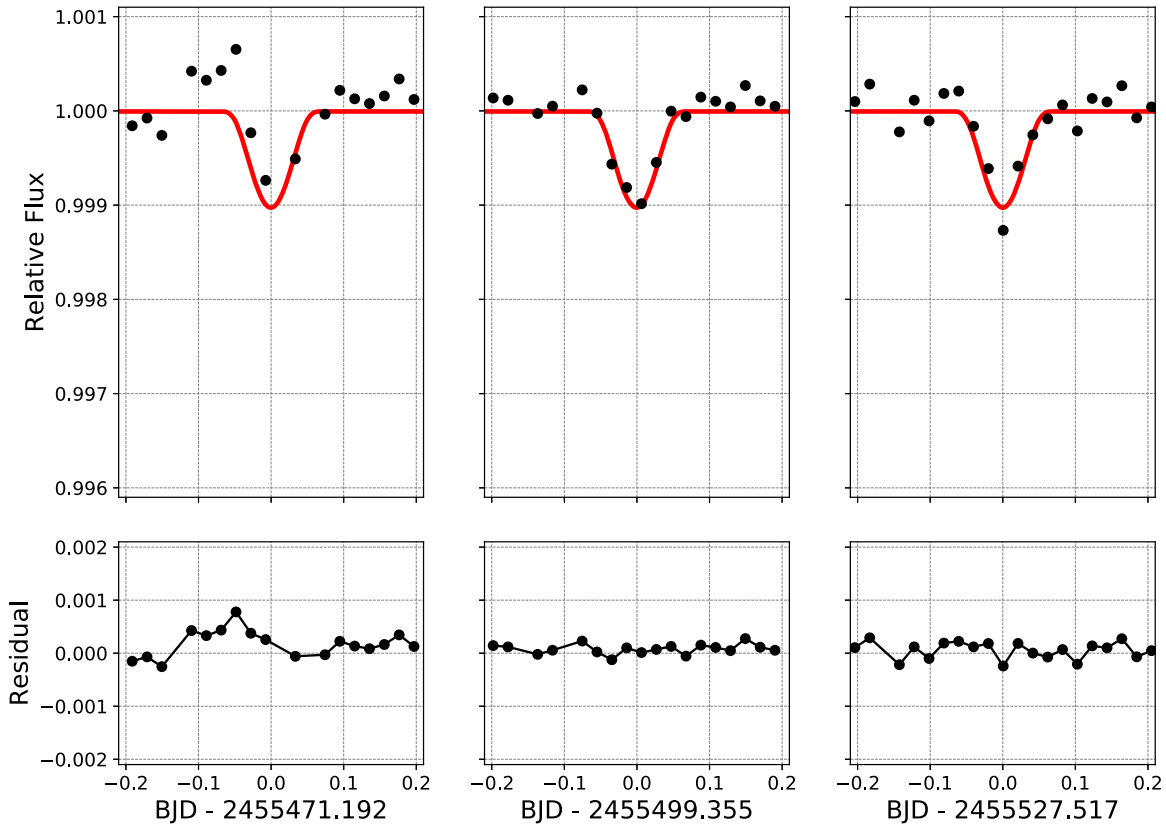

Figure 8. Three examples of secondary eclipses and the best model fit. The noisy, shallow eclipses are a limiting factor in determining the planet mass since the eclipse times cannot be measured with enough precision to allow any meaningful constraint on the $O - C$ diagram.

orbital parameters listed in Tables 2–4 are the instantaneous "osculating" values valid only at the reference epoch and for short times thereafter. In Tables 2 and 3, note that $T_{\rm conj}$ is the time of conjunction with the system's barycenter; for the binary this is approximately the time of mideclipse for the primary, but for the planet it need not be close to an actual transit time. Furthermore, this is the conjunction time based on the orbital elements at the reference epoch; since these evolve with time, the conjunction time will change as well.

4. Discussion

4.1. The Binary

The binary consists of a K and M star in a 28.2 day, mildly eccentric ($e_b = 0.112$) orbit. The stars have masses of 0.84 ± 0.02 and $0.262 \pm 0.005\,M_\odot$, and radii of 0.76 ± 0.01 and $0.276 \pm 0.006\,R_\odot$, consistent with being on the main sequence. Unlike some of the other circumbinary host stars, these stars do not have extremely precise mass and radius determinations, a consequence of having only three transits, all crossing the primary star at close to the same orbital phase. The secondary star is much less luminous than the primary—the ratio of secondary to primary bolometric luminosity is ∼3.3%, and more specifically, it is only 1.1% in the *Kepler* bandpass.

4.1.1. Starspots and Stellar Rotation

The light curve of Kepler-1661 exhibits obvious quasi-periodic modulations that we interpret as being caused by starspots on the primary star. To measure the amplitude and period of the modulations, we first mildly detrend each Quarter to remove instrumental effects. The eclipses and transits were then removed, and any points with Data Quality flags greater than 16 were discarded, along with any obvious outliers and ramps due to the cooling of the photometer. A cubic polynomial was then used to detrend each Quarter. Both the SAP and PDC-MAP data were used in this analysis, and give consistent results. We also used the median of a 50 day wide sliding boxcar for the detrending, and it produced similar results. The SAP light curve is shown in the upper panel of Figure 9. We measure the peak-to-peak amplitude to be 2.5% and the rms variations to be 0.35%. The starspot amplitude in Kepler-1661 is significantly larger than solar fluctuations (∼0.1%), implying a somewhat more active star. Note that the starspot modulation amplitude is not constant—there are intervals when the starspots have very little effect on the light curve.

Assuming the quasi-sinusoidal modulations in the light curve are due to starspots on the primary star, we are able to measure the rotation period of the star. A discrete Fourier transform and a Lomb–Scargle periodogram were used to compute the power spectrum, after a 50% split-cosine bell taper was applied to the detrended light curve. A strong spike at period 24.43 days was found. Harmonics at two and three times the rotation frequency are seen, and a weaker peak is present at the binary orbital frequency (note that this is affected by a sidelobe of the window function of the time series).

Because Fourier techniques assume sinusoidal basis functions, they are not optimal for measuring periods of nonsinusoidal oscillations that change in both amplitude and phase. Hence we prefer to use the autocorrelation function (ACF) to measure the rotation period. However the standard ACF requires continuous data with uniform sampling, so we

Table 2
Kepler-1661 ELC Fitted Parameters

Parameter	Best Fit	1σ	Unit
Binary Star			
Time of Conjunction, $T_{c,b}$	−23.28180	0.00007	BJD–2,455,000
Period, P_b	28.162539	0.00005	days
$\sqrt{e_b}\cos\omega_b$	0.270	0.002	⋯
$\sqrt{e_b}\sin\omega_b$	0.199	0.007	⋯
Inclination, i_b	88.76	0.02	degree
Primary Mass, M_1	0.841	0.022	$M_\odot$
Primary RV Semiamplitude K, K_1	17.30	0.04	km s^{-1}
Primary Radius, R_1	0.762	0.010	$R_\odot$
Ratio of Radii, R_1/R_2	2.756	0.05	⋯
Primary Temperature, T_1	5100	100	K
Temperature Ratio, T_2/T_1	0.71	0.03	⋯
LD Primary *Kepler* q_1	0.93	0.15	⋯
LD Primary *Kepler* q_2	0.05	0.16	⋯
LD Secondary *Kepler* q_1	0.73	0.17	⋯
LD Secondary *Kepler* q_2	0.93	0.24	⋯
LD Primary MLO (R) q_1	0.52	0.20	⋯
LD Primary MLO (R) q_2	0.33	0.22	⋯
Planet			
Mass, M_p	17	12	$M_\oplus$
Radius Ratio with Primary Star, R_1/R_p	21.50	0.33	⋯
Time of Conjunction, $T_{c,p}$	1007.1	0.4	BJD–2,455,000
Period, P_p	175.06	0.07	days
$\sqrt{e_p}\cos\omega_p$	0.092	0.023	⋯
$\sqrt{e_p}\sin\omega_p$	0.219	0.009	⋯
Inclination, i_p	89.464	0.012	degree
Nodal Longitude, Ω_p	0.61	0.03	degree

Table 3
Kepler-1661 System Parameters

Parameter	Best Fit	1σ	Unit
Primary Star			
Primary Mass, M_1	0.841	0.022	$M_\odot$
Primary Radius, R_1	0.762	0.010	$R_\odot$
Primary Temperature, T_1	5100	100	K
Secondary Star			
Secondary Mass, M_2	0.262	0.005	$M_\odot$
Secondary Radius, R_2	0.276	0.006	$R_\odot$
Secondary Temperature, T_2	3585	167	K
Planet			
Planet Mass, M_p	17	12	$M_\oplus$
Planet Radius, R_p	3.87	0.06	$R_\oplus$
Average Density, ρ_p	1.6	1.1	g cm^{-3}
Binary Orbit at BJD = 2,454,960			
Period, P_b	28.162539	0.00005	days
Time of Conjunction, $T_{c,b}$	−23.28180	0.00007	BJD–2,455,000
Semimajor Axis of Binary, a_b	0.187	0.002	au
Eccentricity, e_b	0.112	0.002	⋯
Argument of Periastron, ω_b	36.4	1.1	degree
Inclination, i_p	88.76	0.02	degree
Primary Impact Parameter, b_1	0.755		⋯
Secondary Impact Parameter, b_2	0.862		⋯
Planet Orbit at BJD = 2,454,960			
Orbital Period, P_p	175.06	0.06	days
Time of Barycenter Conjunction, T_c, p	1007.1	0.4	BJD–2,455,000
Semimajor Axis, a_p	0.633	0.005	au
Eccentricity, e_p	0.057	0.005	⋯
Argument of Periastron, ω_p	67.1	5.0	degree
Inclination, i_p	89.46	0.02	degree
Nodal Longitude, Ω_p	0.61	0.03	degree
Mutual Inclination, Δi	0.93	0.02	degree

patched small gaps with a linear interpolation and patched larger gaps (e.g., when Kepler-1661 was on a bad CCD module) with a random walk whose amplitude was scaled to match that of the light curve. We then created 100 realizations of the patched light curve and computed the ACF for each, then averaged. The result is shown in the bottom panel of Figure 9. The peak of the ACF occurs at a period of 24.44 days. To estimate the uncertainty on the period, we also used the second, third, and fourth peaks in the ACF, dividing their periods by 2, 3, and 4. We then computed the weighted mean using the inverse of the correlation coefficient as the weight, and measured the standard deviation of the set. This is similar, but not identical to, the method described in McQuillan et al. (2013). In particular, more weight is put on the first ACF peak. We repeated the above using the PDC-MAP light curve, and as a final sanity check, we also patched the light curve using pure white noise consistent with the rms scatter of the light curve. All results were consistent with each other, and with the Fourier methods. We adopt as our final stellar rotation period estimate 24.44 ± 0.08 days.

The measured stellar rotation period is less than the binary period, and more importantly, less than the 26.17 day pseudosynchronous period for an eccentric orbit (Hut 1981) —see Figure 9. However, this is not unexpected: for a 28 day period binary, the timescale for spin synchronization is over 25 Gyr (and much, much longer for orbital circularization).

Using the measured rotation period and the estimate for the radius of the star, the expected $V_{\rm rot}\sin i$ is 1.6 km s^{-1}, assuming the spin axis is perpendicular to the orbital plane and that the effects of any differential rotation are negligible. The observed $V_{\rm rot}\sin i$ from the two highest signal-to-noise spectra is $\sim 2.5 \pm 0.5$ km s^{-1}, slightly higher than the estimate using the star's spin period.

4.1.2. Comparison with Stellar Isochrones

In Figure 10 we compare the MCMC posterior sample with the PARSEC isochrones (Bressan et al. 2012). The color of the points corresponds to the density of the points in the figure, with blue being low density and yellow high density. The primary star appears to be a relatively young star, ∼1–3 Gyr, though there are some solutions in the posterior that extend up to 8 Gyr (although with low probability). A young age is consistent with the starspot activity on the star. A more solar-like metallicity is preferred than the nominal [Fe/H] = −0.12, and even higher-than-solar metalicities are favored if the stellar temperature is on the low end of its measured range. The secondary star's radius is larger than expected; this is not unusual for stars of this mass (e.g., see the review by Torres et al. 2010). The temperature is also higher than expected, and

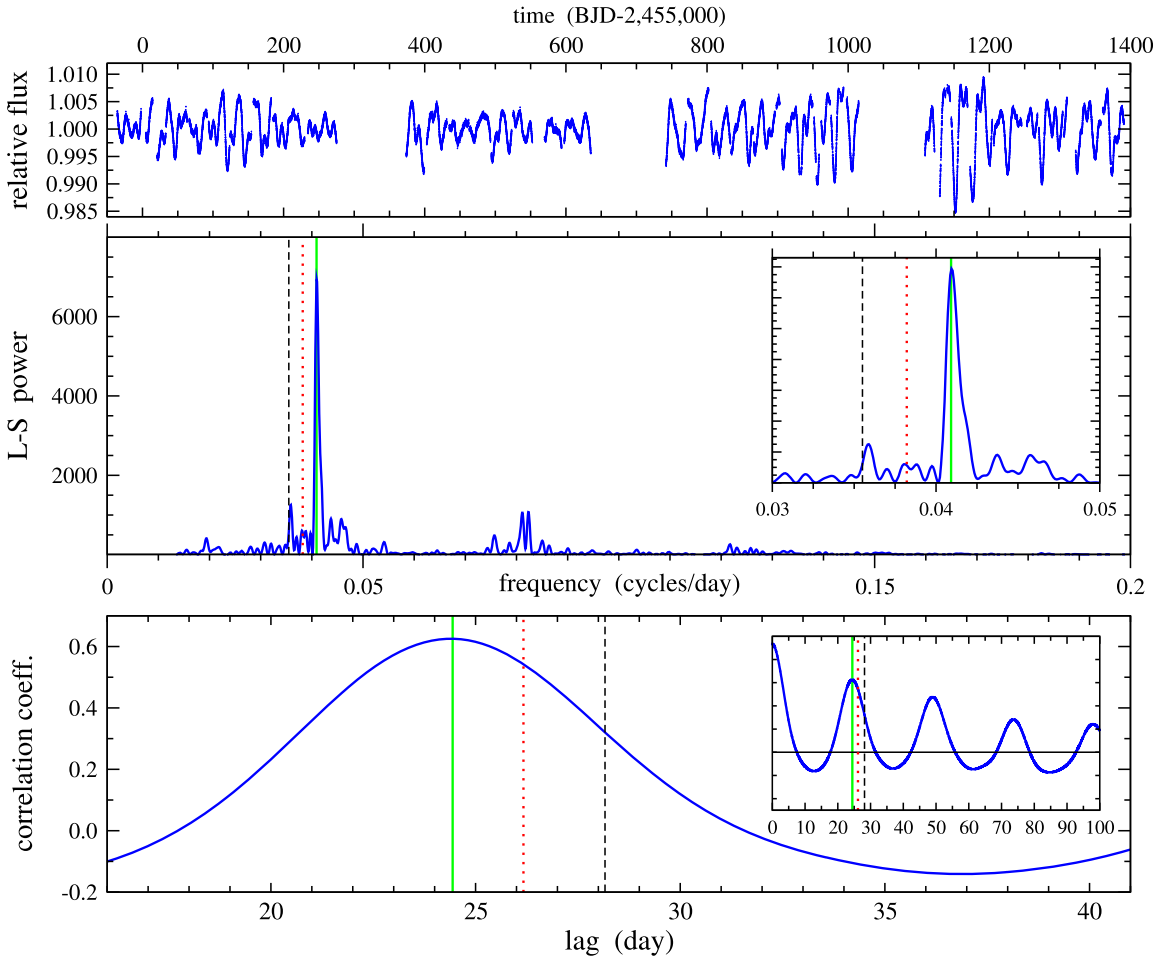

Figure 9. The upper panel shows the detrended and normalized light curve for Kepler-1661. Starspot modulations are readily seen, and their amplitude is not constant over the 4 yr of *Kepler* data. The large ∼90 day gaps are due to the target falling on one of the failed CCD modules. The middle panels show the Lomb–Scargle power spectrum (the inset shows a zoomed-in version), with the black dashed line marking the orbital frequency, the red dotted line marking the pseudosynchronous frequency, and the green line marking the stellar spin frequency. The lower panels show the autocorrelation function (the inset shows a zoomed-out version). The orbital, pseudosynchronous, and spin periods are shown.

Table 4
Kepler-1661 Barycentric Cartesian Positions and Velocities at BJD = 2,454,960

Parameter	Primary Star	Secondary Star	Planet
Mass, $M_\odot$	8.40853449093473149E-01	2.62347276214166703E-01	5.11075180194982723E-05
x, au	3.53188589024455990E-02	−1.13185968929754660E-01	−7.73598863314166052E-02
y, au	7.47539718007338670E-04	−2.39687876159461882E-03	4.75985351132452317E-03
z, au	3.46026030406624344E-02	−1.11021524038963662E-01	5.96317715973122775E-01
V_x, au day^{-1}	−6.32910801823011269E-03	2.02901512397735267E-02	−2.37461133149127167E-02
V_y, au day^{-1}	1.34484593955837620E-04	−4.30985153500305885E-04	−2.74980447028744235E-04
V_z, au day^{-1}	6.22776497258325894E-03	−1.99602373233647816E-02	−2.42161959431956781E-03

this is somewhat atypical, though there is large uncertainty in the temperature.

4.2. The Planet

4.2.1. Planet Characteristics

The *Kepler* light curve contains three transits across the primary star, substantially fewer than the eight that could potentially have been detected given the 175 day period of the planet. However, three full Quarters of data are missing (plus Quarter 17) because of the failed CCD module, and the planet's impact parameter was greater than 1.0 prior to the third year of observations. In addition, a transit that could have been detected in Quarter 16 fell in a small data gap. No transits over the secondary are detected, although the nondetection of any such transits is fully consistent with the secondary star being much fainter than the primary. The three transits do provide enough information to characterize the planet fairly well, though much of the uncertainty is propagated from uncertainty in the binary star parameters. The planet's radius ($3.87 \pm 0.06\,R_\oplus$) is well determined and similar to Neptune's ($3.88\,R_\oplus$). The mass, however, is much less well determined:

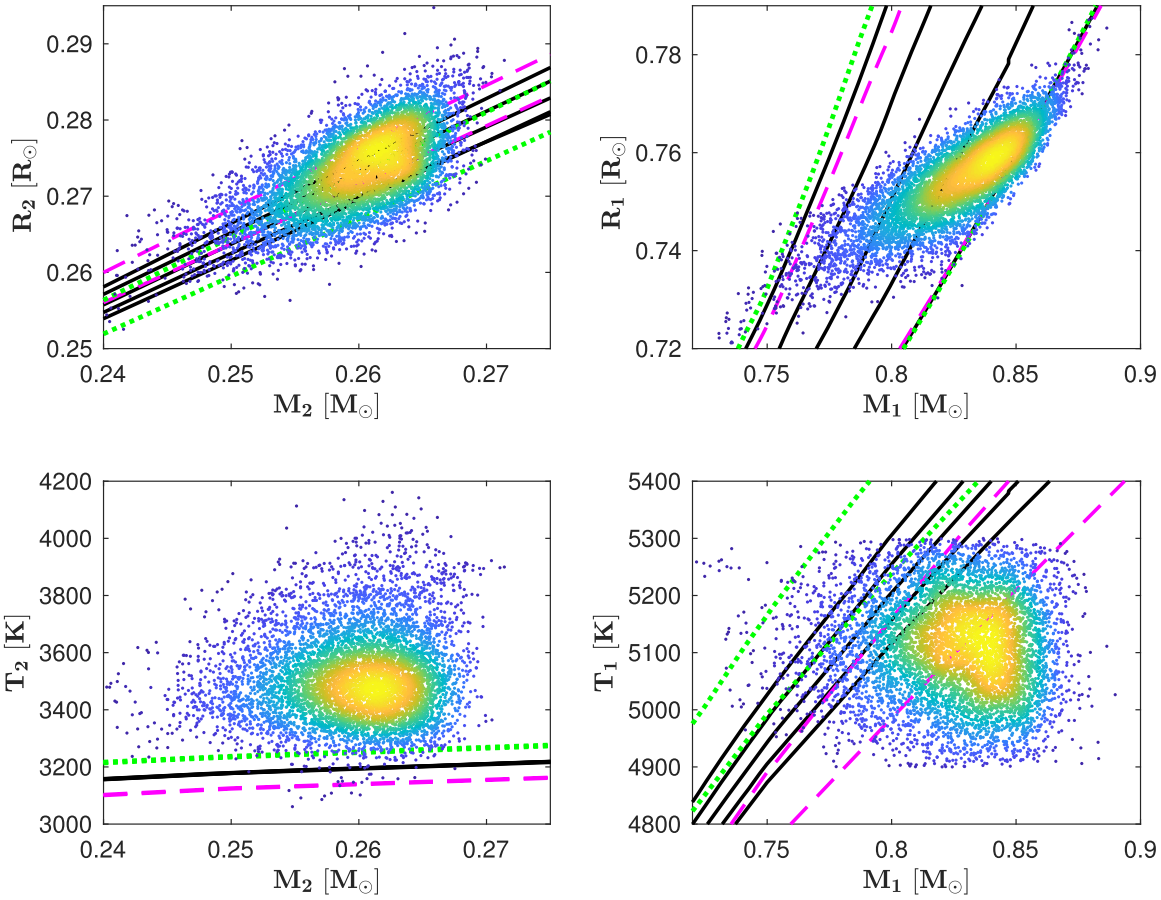

Figure 10. The set of masses, radii, and temperatures from the MCMC posterior sample for the secondary star (left panels) and primary star (right panels) are plotted, along with the PARSEC isochrones (Bressan et al. 2012). The solid black curves from bottom to top are the 1, 3, 5, 7, and 9 Gyr isochrones for the nominal metallicity of [Fe/H] $= -0.12$. The dashed magenta curves bracket the 1–9 Gyr isochrones for a metallicity of -0.02, and the dotted green curves are for a metallicity of -0.22.

$17 \pm 12\,M_{\oplus}$. This is a consequence of the weak constraint placed by the ETVs. The ETVs, expressed in a common-period $O - C$ diagram is shown in Figure 11. The secondary times are very noisy due to the shallow secondary eclipses, and this prevents any useful mass constraint based on an induced apsidal motion of the binary. The main mass constraint is therefore based on the "ripples" in the $O - C$ diagram, caused by the dynamical perturbation of the binary by the planet (Borkovits et al. 2011, 2015). While small, the effect the planet has on the binary still dominates over the general relativistic precession (which accounts for 17% of the precession) and the classical apsidal motion due to tidal interaction (less than 1%). Given the small amplitude of the $O - C$ variations, it is perhaps more correct to say that it is the *lack* of ETVs that provides an upper limit constraint on the planet's mass. This is illustrated in Figure 11 where the orange curve shows the expected $O - C$ variations for a planet of 1 $M_{\rm Jup}$. The variations from a planet of this mass are larger than the observed variations, thus the planet is of lower mass. The blue curve shows the photodynamical model best-fit variations, and while not a particularly good match, it is much more consistent with the amplitude of the variations. Despite the low-precision mass determination, the conclusion is robust: the circumbinary object in Kepler-1661 is substellar. With three transits that match in detail the times, depths, and durations expected of a circumbinary object, the candidate's planethood is established.

4.2.2. Orbital Characteristics

The planet's orbit is mildly eccentric ($e_p \approx 0.057$) and resides nearly coplanar ($\Delta i \sim 1^{\circ}$) with the binary orbital plane, which is consistent with the orbital properties of all the known transiting *Kepler* CBPs (Li et al. 2016). The planetary orbital period ($P_p = 175.06 \pm 0.06$) is ~6.2 times the binary orbital period. Using the stability criteria from Holman & Wiegert (1999), we find the ratio $P_p/P_{\rm crit} = 1.381$ indicating that the planet is on the stable side of the so-called stability limit. The period ratio between the innermost planet and the binary is an interesting characteristic of many *Kepler* CBPs, and Welsh & Orosz (2018) note this ratio is close to unity for many CBP systems. In terms of the planetary semimajor axis ratio $a_p/a_{\rm crit}$ (=1.281), the planet also appears to be near the stability limit. However, the Holman & Wiegert (1999) analysis produces a stability formula that is averaged over several parameters, where the stability limit can be over- or underestimated when compared to n-body simulations of specific systems. In this case, the Holman & Wiegert (1999) criterion overestimates the critical period $P_{\rm crit}$ for stability and hence the ratio $P_p/P_{\rm crit}$ is larger (~1.434) if more sophisticated analyses are used (Lam & Kipping 2018; Quarles et al. 2018). These analyses are generally applicable for planets on near circular and coplanar orbits, but Quarles et al. (2018) provides an empirical relationship for the maximum eccentricity for a planet as a function of its semimajor axis ratio ($e_{\rm max} \approx 0.2$ for Kepler-1661) before it becomes unstable due to the overlap of N:1

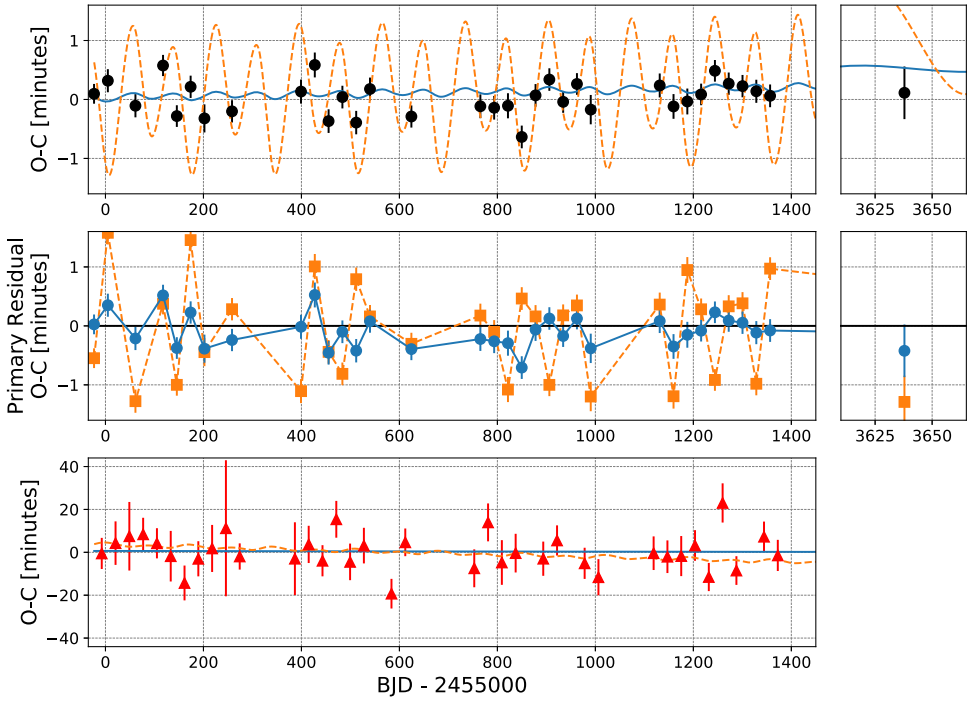

Figure 11. The observed-minus-calculated $O - C$ mideclipse times for the *Kepler* primary eclipses (top panel) and secondary eclipses (bottom panel) after the best-fit, common linear ephemeris has been subtracted. The upper right-hand panel corresponds to the MLO primary eclipse. The blue curve is the best-fit 17 $M_{\oplus}$ model prediction. The dotted orange curve is the best-fit model for a 1 $M_{\rm Jup}$ planet. The middle panel shows the residual primary eclipse times against the models shown in the upper panel, with the blue circles being the residuals of the nominal 17 $M_{\oplus}$ model and orange squares for the residuals of the 1 $M_{\rm Jup}$ model for the mass of the planet. While the primary eclipse times are noisy and are not particularly well matched by the nominal model, the Jupiter-mass model is much worse (χ^2 of 79 vs. 594 with 25 fitting parameters and 34 data points).

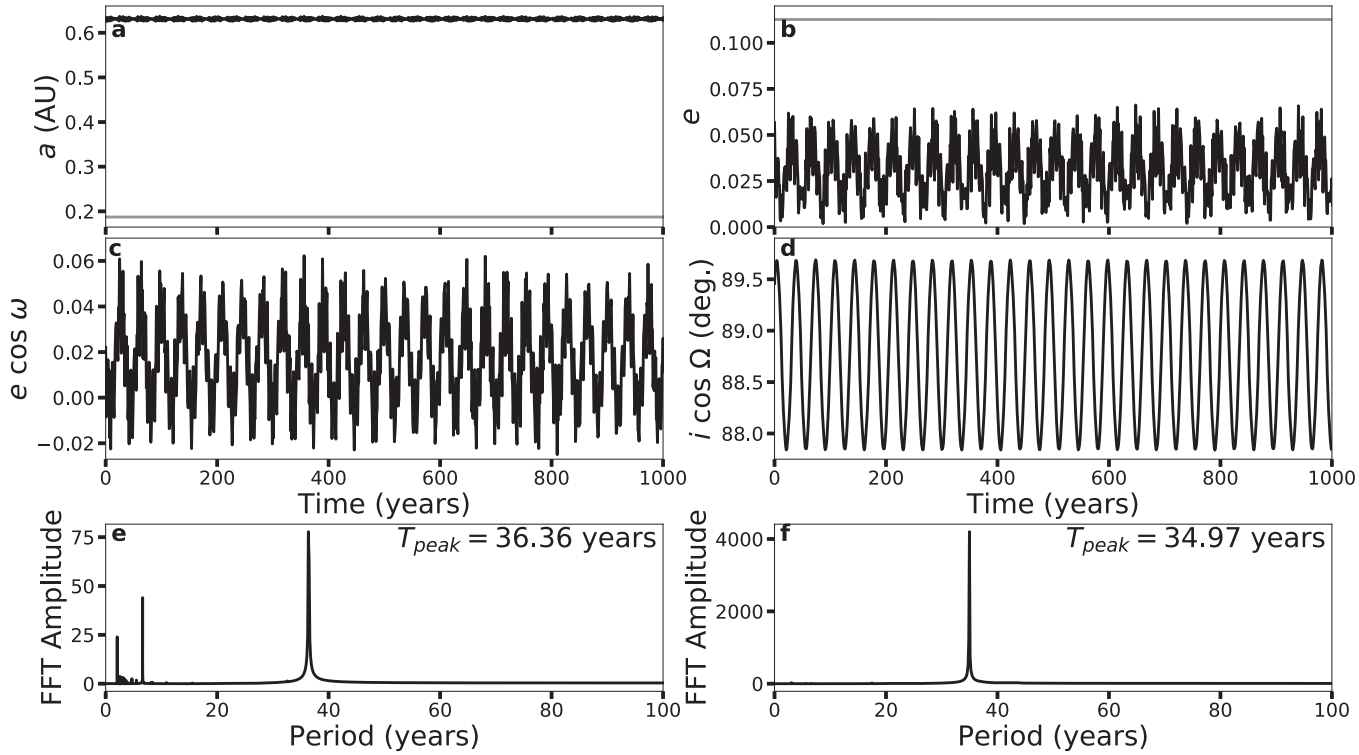

Figure 12. Orbital evolution for 1000 yr starting from BJD = 2,454,960 of the semimajor axis (panel (a)), and the eccentricity (panel (b)), for the planet and binary (black curve and gray curve, respectively). The evolution for the x-component in the (c) eccentricity $e\cos\omega$ and (d) inclination $i\cos\Omega$ vector is given, along with a periodogram showing the periods of (e) apsidal precession from $e\cos\omega$ and (f) nodal precession from $i\cos\Omega$.

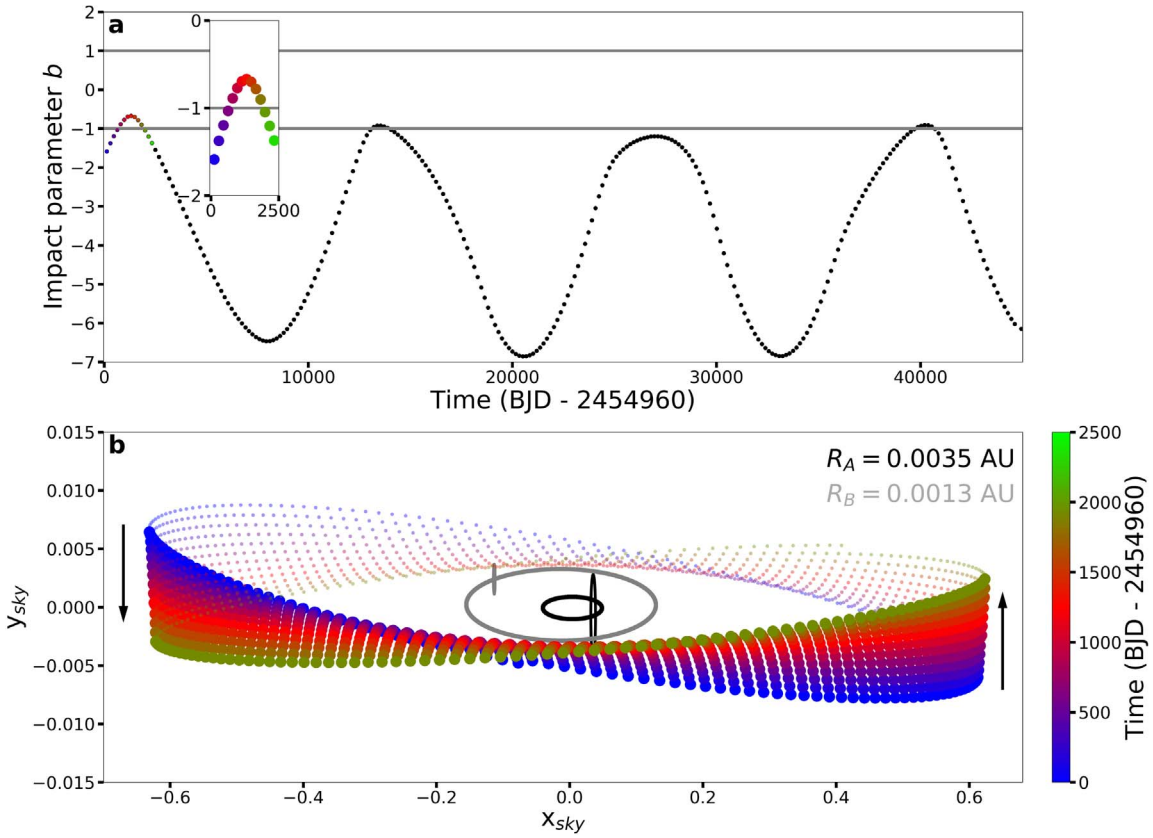

Figure 13. The effect of nodal precession on the impact parameter b is shown in the upper panel (a), over the span of 45,000 days. Only for those conjunctions with $|b| < 1$ do transits occur, as denoted by the horizontal gray lines. The long-term oscillations in the impact parameter limit the transit-ability of Kepler-1661, where some parts of the precession cycle prohibit transits (e.g., near time ∼27,000 days). The inset shows a zoomed-in view of the first 2500 days, where only 7 transits are possible. Panel (b) shows the plane of the sky alignment of the planet and binary and illustrates how the orbit of the planet tilts due to nodal precession. The points are color-coded with respect to the time in days, which spans a range of 2500 days, or about 20% of a precession cycle. The cross section of stellar disk for star A (black) and star B (gray) are shown as thin hoops, stretched vertically because of the very different y-axis scale. The other two ellipses show their orbits. The transparency of the points indicate the z-component of the planetary orbit on the sky plane, where the smaller, faint, semitransparent points lie into the page (behind the barycenter).

mean motion resonances with the binary (Mudryk & Wu 2006; Sutherland & Kratter 2019). The best-fit planetary eccentricity could triple and remain below the threshold for eccentricity, which further enhances the evidence for a stable orbit.

Another definition for a CBP to be at the stability limit is to check if another planet of equal mass is allowed in between the known planet's orbit and $a_{\rm crit}$. We use a planet-packing formalism that uses the dynamical spacing β between planets (Chambers et al. 1996; Kratter & Shannon 2014; Quarles et al. 2018), where $\beta \geqslant 7$ indicates that an equal-mass nearby planet with semimajor axis $a_{\rm crit}$ would also be stable. Using the stability fitting formula from Holman & Wiegert (1999), we find $\beta \approx 7.28$ which demonstrates that although this planet is near the stability limit, it still allows for a stable interior planet. Furthermore, we can use the more recent approaches and find that the spacing of the planet relative to the stability limit increases, where $\beta \approx 9.18$ using the machine learning method (Lam & Kipping 2018) and $\beta \approx 8.21$ using the grid interpolation method (Quarles et al. 2018).

We dynamically integrated the system orbits using the IAS15 integrator in the REBOUND code (Rein & Liu 2012; Rein & Spiegel 2015), starting with the parameters listed in Tables 3 and 4. Our 100,000 yr simulation revealed small oscillations in the planetary semimajor axis, eccentricity, and inclination, where the maximum eccentricity and inclination was 0.066 and $1^{\circ}.57$, respectively. Figure 12 shows the evolution of the planetary (black) and binary (gray) semimajor axes and eccentricity for the first 1000 yr. We also show the evolution for the x-component (middle panels) of the planetary eccentricity $e\cos\omega$ and inclination vector $i\cos\Omega$ along with the corresponding periodogram (bottom panels) that illustrate the planetary apsidal and nodal precession periods. Although the two precession periods are similar in the case of Kepler-1661, the 35 yr nodal precession period is more relevant for transits. A result of the rapid precession of the planet's orbit is clearly seen in Figure 2, where the transit depth and width increase on subsequent transits. Such a rapid precession is not unusual for CBPs, where Kepler-413 has a remarkably short 11 yr precession timescale (Kostov et al. 2014). A consequence of the nodal precession is that the orbital inclination, and hence the impact parameter, b, is continuously changing. Figure 13 shows the variation in impact parameter, ranging from −6.8 to −0.67, over the course of 45,000 days or ∼3.5 precession periods. Interestingly, as the planet's orbit precesses, the plane of the planet tilts up from below the binary plane to cross the primary, but it never gets as high as the equator before precessing back down off the star. The planet can only transit the host star if $|b| < 1$, and as can be seen in Figure 13, this is a small part of the curve. The fraction of time in a precession cycle that the planet is sufficiently aligned with our line of sight to enable transits is only ∼7% on average, noting that one out of every four precession cycles results in no observable transits.

Table 5
Kepler-1661 Predicted Transits of the Planet across the Primary Star

Date			UT	BJD–2,455,000	Impact Parameter	Duration (days)
2009	May	3	7:22:04.8	$-45.193^{+0.033}_{-0.031}$	$-1.673^{+0.038}_{-0.041}$	…
2009	Oct	20	3:41:45.6	$124.654^{+0.023}_{-0.023}$	$-1.486^{+0.027}_{-0.040}$	…
2010	Apr	8	1:33:36.0	$294.565^{+0.015}_{-0.017}$	$-1.319^{+0.029}_{-0.024}$	…
2010	Sep	25	1:11:08.2	$464.5494^{+0.0082}_{-0.0104}$	$-1.149^{+0.020}_{-0.016}$	…
2011	Mar	14	2:57:15.8	$634.6231^{+0.0028}_{-0.0058}$	$-0.9911^{+0.0099}_{-0.0168}$	$0.058^{+0.026}_{-0.019}$
2011	Aug	31	7:13:09.1	$804.8008^{+0.0014}_{-0.0019}$	$-0.8578^{+0.0086}_{-0.0077}$	$0.2186^{+0.0054}_{-0.0065}$
2012	Feb	17	14:19:58.1	$975.0972^{+0.0013}_{-0.0013}$	$-0.7489^{+0.0105}_{-0.0067}$	$0.3103^{+0.0033}_{-0.0056}$
2012	Aug	6	0:10:56.6	$1145.5076^{+0.0019}_{-0.0013}$	$-0.672^{+0.013}_{-0.015}$	$0.3724^{+0.0047}_{-0.0072}$
2013	Jan	23	11:52:04.8	$1315.9945^{+0.0062}_{-0.0042}$	$-0.649^{+0.025}_{-0.020}$	$0.3979^{+0.0069}_{-0.0113}$
2013	Jul	12	23:30:46.1	$1486.4797^{+0.0092}_{-0.0107}$	$-0.676^{+0.035}_{-0.029}$	$0.372^{+0.014}_{-0.013}$
2013	Dec	30	8:45:36.0	$1656.865^{+0.017}_{-0.012}$	$-0.755^{+0.043}_{-0.035}$	$0.308^{+0.019}_{-0.021}$
2014	Jun	18	14:32:38.4	$1827.106^{+0.018}_{-0.026}$	$-0.871^{+0.050}_{-0.041}$	$0.210^{+0.032}_{-0.029}$
2014	Dec	5	16:22:04.8	$1997.182^{+0.029}_{-0.030}$	$-0.997^{+0.046}_{-0.056}$	$0.104^{+0.035}_{-0.048}$
2044	Sep	4	4:48:00.0	$12862.7^{+2.0}_{-2.7}$	$-1.092^{+0.061}_{-0.085}$	$0.096^{+0.016}_{-0.054}$
2045	Feb	21	16:48:00.0	$13033.2^{+2.0}_{-2.6}$	$-0.975^{+0.049}_{-0.063}$	$0.140^{+0.073}_{-0.059}$
2045	Aug	11	4:48:00.0	$13203.7^{+1.9}_{-2.4}$	$-0.900^{+0.064}_{-0.049}$	$0.229^{+0.049}_{-0.074}$
2046	Jan	28	9:35:60.0	$13373.9^{+1.9}_{-2.1}$	$-0.825^{+0.047}_{-0.100}$	$0.272^{+0.040}_{-0.104}$
2046	Jul	17	12:00:00.0	$13544.0^{+1.6}_{-1.7}$	$-0.838^{+0.095}_{-0.092}$	$0.169^{+0.098}_{-0.075}$
2047	Jan	3	14:24:00.0	$13714.1^{+1.3}_{-1.7}$	$-0.910^{+0.127}_{-0.077}$	$0.128^{+0.091}_{-0.065}$
2047	Jun	22	9:35:60.0	$13883.9^{+1.3}_{-1.3}$	$-0.948^{+0.110}_{-0.083}$	$0.101^{+0.092}_{-0.052}$
2047	Dec	9	4:48:00.0	$14053.7^{+1.2}_{-1.5}$	$-1.013^{+0.108}_{-0.059}$	$0.086^{+0.072}_{-0.052}$
2048	May	27	0:00:00.0	$14223.5^{+1.0}_{-1.4}$	$-1.050^{+0.078}_{-0.080}$	$0.061^{+0.068}_{-0.036}$
2048	Nov	12	14:24:00.0	$14393.1^{+1.0}_{-1.3}$	$-1.133^{+0.087}_{-0.060}$	$0.089^{+0.047}_{-0.060}$

Note. The transits at 2011 August 31, 2012 February 17, and 2012 August 6 were observed during the *Kepler* mission.

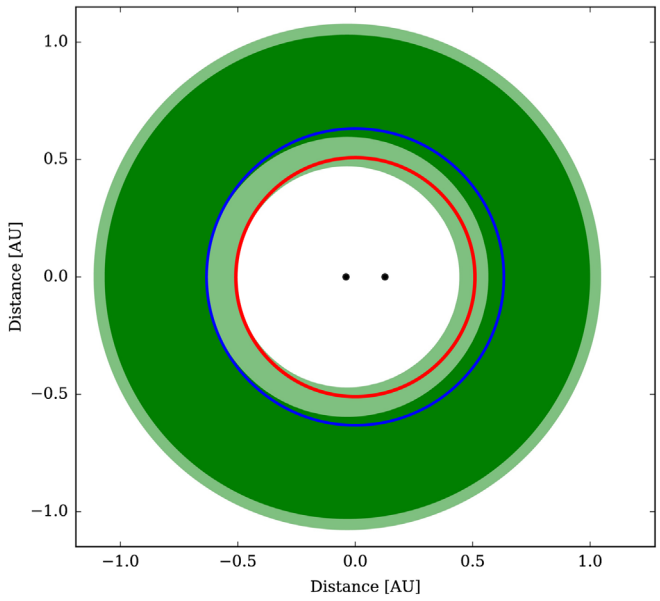

Figure 14. Face-on view of the Kepler-1661 system, showing the planet's orbit (in blue) relative to the binary and the habitable zone. The dark green region corresponds to the narrow (conservative) habitable zone, and the light green corresponds to the nominal (extended) habitable zone as defined by Kopparapu et al. (2013a, 2013b). The critical radius for stability is shown in red.

In Figure 13 we also show how the planet's orbital plane tilts on the plane of the sky over the first 2500 days (color-coded), which further demonstrates the rarity of alignments that allow for transits. At the current time, the planet is no longer transiting. The next cycle of transits is expected to start in 2045. See Table 5 for the predicted times, impact parameters, and durations of future transits. These are for the best-fit model, but of course there is a spread of acceptable solutions, so there is a range of values for the items in the table.

4.2.3. Habitable Zone

In general, the *Kepler* CBPs that are located near the orbital dynamical instability limit are often near their classical stellar-heated habitable zones. Kepler-1661 is no exception. Although its mass and radius suggest a "warm Neptune" planet that is not conducive to life as we know it, it is still interesting to estimate the amount of radiant energy the planet receives and compare this with the habitable zone.

The K-star primary dominates the energy output of the stars, allowing a first-order approximation to the incident stellar flux on the planet's atmosphere to be easily computed. The orbit-averaged insolation at the reference epoch is 0.88 $S_\oplus$ where $S_\oplus$ is the Sun–Earth insolation (equal to 1367 W m^{-2}). This insolation is less than the conservative "moist greenhouse" upper limit of 0.961 $S_\oplus$ for the hotter inner edge of the habitable zone and well within the more optimistic runaway greenhouse or recent Venus limits (see Kopparapu et al. 2013a, 2013b, and the 2014 online updated coefficients[8]). Assuming a Bond albedo of 0.34 and that the planet re-emits the absorbed radiation over a full sphere, the planet's equilibrium temperature $T_{\rm eq}$ is ∼243 K. A face-on view of the Kepler-1661 system is shown in Figure 14, created with the web-based software Multiple Star HZ calculator[9] described in Müller & Haghighipour (2014). The darker green region corresponds to the conservative habitable zone and the lighter green corresponds to the optimistic

[8] http://depts.washington.edu/naivpl/content/hz-calculator
[9] http://astro.twam.info/hz/

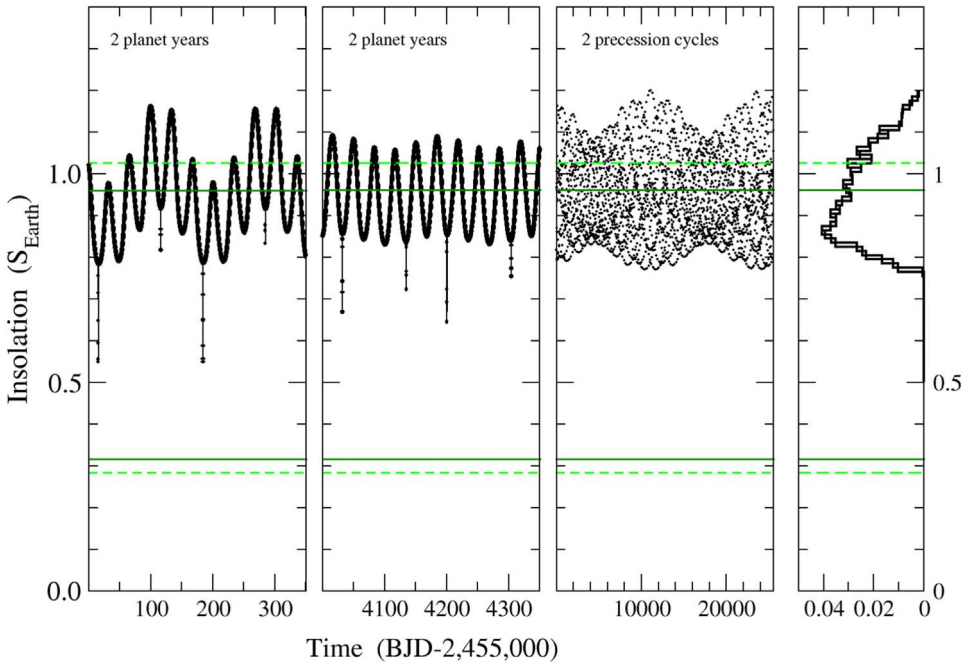

Figure 15. The insolation incident at the top of the atmosphere for Kepler-1661, in units of the Sun–Earth insolation. Left panels: the fluctuations in the insolation over a period of two planet orbits (2 × 175.4 days) during the *Kepler* epoch. The dashed green lines mark the boundaries of the habitable zone as defined by Kopparapu et al. (2013a) and Kopparapu et al. (2013b). The sharp downward spikes are due to the stellar eclipses as seen from the planet. Middle-left panel: the insolation at an epoch where the fluctuations are less extreme. Middle-right panel: the distribution of the insolation over two apsidal precession cycles of the planet (equal to ∼70 yr). Right panel: a histogram of the long-term distribution of the insolation.

habitable zone. The red circle marks the (in)stability radius based on the Holman & Wiegert (1999) formula.

Integrating the equations of motion for the three bodies allows us to compute the exact instantaneous insolation, and enable us to follow it though a precession cycle. Figure 15 shows the insolation from both stars as a function of time. The shortest timescale variation (∼28 days) is caused by the orbital motion of the primary star. Variations due to the planet's eccentric orbit are present at a timescale of the orbital period of the planet. On a much longer timescale are fluctuations caused by the precession of the orbits (∼35 yr). The precession causes the peak-to-peak fluctuations in insolation over the course of the planet's year to vary cyclically. The average insolation over the full precession cycle is $\langle S \rangle = 0.947$, with an rms fluctuation of 10.4%. The median and the mode are slightly lower, at 0.936 and 0.865, respectively. These long-term averages are just within the conservative HZ limit (set by the moist greenhouse criteria), though excursions above that limit, and even above the runaway greenhouse limit, are present for a substantial amount of time—see the histogram in the last panel of Figure 15.

5. Conclusion

In this study, we report the discovery of a transiting CBP of approximately Neptune mass and radius in a nearly coplanar orbit around a K + M eclipsing binary. The planet orbits near the critical stability radius and is, on average, inside the habitable zone. The host binary is a single-lined spectroscopic binary but the planet transits can, in theory, provide enough information to determine the absolute masses, radii, and geometry of the system. Unfortunately, in Kepler-1661 only three transits across the primary star were observed and they all occur near the same binary phase, and thus provide only limited constraints on the primary star's position and velocity. No transits were observed across the secondary. However, by steering the photodynamical modeling solutions to agree with stellar isochrone models, enough information is available to determine a full set of system parameters. Care must be taken in the modeling because the eclipses of the stars are grazing (high impact parameter), making them particularly sensitive to the orbital inclination. The planet causes the binary's orbit to precess, which causes the inclination to change, which in turn causes the eclipse depths to change. But starspots create modulations in the light curve, and the standard procedure for detrending and normalizing *Kepler* data can also result in (spurious) changes in eclipse depth.

A ground-based observation of a primary eclipse was obtained in 2019 and was extremely valuable because it more than doubled the temporal baseline of the time series. This allowed a much better determination of the effect the planet has on the binary. The precession period is 35 yr, and the planet spends only ∼7% of the time in a configuration where transits are detectable from our line of sight. The transits which began in 2011 ended in 2014, and the next cycle of observable transits is not expected to start until 2045. Thus no transits are expected during the *TESS* Primary Mission.

We thank the anonymous reviewer for suggestions and comments that have improved this paper. We gratefully acknowledge support from the National Science Foundation via award AST-1617004, and we are are also deeply grateful to John Hood, Jr. for his generous support of exoplanet research at SDSU. We acknowledge years of fruitful discussion with members of the *Kepler* TTV/Multi-Planet Working Group and Eclipsing Binaries Working Group. In particular we would like to thank Josh Carter for initial work on this CBP system. We also thank Andre Prsa, Kelly Hambleton, Kyle Conroy (Villanova Univ.), and Tara Fetherolf and Trevor Greg (SDSU

undergraduates at the time) for their assistance in acquiring the KPNO spectra. *Kepler* was competitively selected as the 10th mission of the Discovery Program. Funding for this mission is provided by NASA, Science Mission Directorate. The Hobby–Eberly Telescope (HET) is a joint project of the University of Texas at Austin, the Pennsylvania State University, Ludwig-Maximilians-Universität München, and Georg-August-Universität Göttingen. The HET is named in honor of its principal benefactors, William P. Hobby and Robert E. Eberly. This research has made use of the Exoplanet Follow-up Observation Program website and the NASA Exoplanet Archive, which are operated by the California Institute of Technology, under contract with the National Aeronautics and Space Administration under the Exoplanet Exploration Program. This work is also based in part on observations at Kitt Peak National Observatory, National Optical Astronomy Observatory, which is operated by the Association of Universities for Research in Astronomy (AURA) under a cooperative agreement with the National Science Foundation. Simulations in this paper made use of the REBOUND code which is freely available at http://github.com/hannorein/rebound.

Facilities: Kepler, Smith (Tull spectrograph), HET (HRS spectrograph), Mayall (Echelle spectrograph), MLO:1 m.

Software: AstroImageJ (Collins et al. 2017).

Appendix
Attempted Debiasing of the Primary Eclipses

In an attempt to correct the eclipse depth bias, we measured the peak-to-peak amplitude of the starspot modulation in the normalized (but not detrended) light curve. The peak-to-peak amplitude in a sliding boxcar of width 50 days (roughly twice the stellar rotation period—see Section 4.1.1) was used to provide slight smoothing of the variations. Figure 5 shows the light curve, the starspot modulation amplitude, and the actual measured depth of each primary eclipse. The starspot amplitude time series, $A(t)$, was then used to correct the usual normalized and detrended light curve $D(t)$ to produce a de-biased data:

$$D' = D - A(D - 1). \quad (1)$$

The amplitude correction term A ranges from 0.5% to 2.5%, and the larger the starspot amplitude, the more the eclipse depth is decreased. The eclipse depths after this debiasing no longer had a long-term tilt, but small eclipse-to-eclipse variations were still present.

The result of using the de-biased light curve was a noticeable decrease in best-fit value for the planet mass. Yet the mass still remained abnormally high, $\sim 70\,M_{\oplus}$, and the model still preferred a higher primary star mass than expected. So unfortunately this simple prescription for the debiasing was insufficient to yield a satisfactory solution. The debiasing method was abandoned for the more straightforward method described in Section 3.4, but not without exploring one more attempt to find a method that gave a sensible planet mass. For this approach we renormalized all the primary eclipses to the same level in flux, 0.9628 (a depth of 3.72%), which is the average depth that was observed during the times of the least starspot activity. By construction this removes sensitivity to the eclipse depth variations, and leaves only the ETVs as the source of constraining the planet's mass. This method has limitations, but it was useful as a check. The resulting parameter estimates agreed to within 1σ with the adopted method described in Section 3.4.

ORCID iDs

Quentin J Socia https://orcid.org/0000-0002-7434-0863
William F Welsh https://orcid.org/0000-0003-2381-5301
Jerome A Orosz https://orcid.org/0000-0001-9647-2886
William D Cochran https://orcid.org/0000-0001-9662-3496
Michael Endl https://orcid.org/0000-0002-7714-6310
Billy Quarles https://orcid.org/0000-0002-9644-8330
Guillermo Torres https://orcid.org/0000-0002-5286-0251
Gur Windmiller https://orcid.org/0000-0002-6742-4911

References

Borkovits, T., Csizmadia, S., Forgács-Dajka, E., & Hegedüs, T. 2011, A&A, 528, A53
Borkovits, T., Rappaport, S., Hajdu, T., & Sztakovics, J. 2015, MNRAS, 448, 946
Bressan, A., Marigo, P., Girardi, L., et al. 2012, MNRAS, 427, 127
Casagrande, L., Ramírez, I., Meléndez, J., et al. 2010, A&A, 512, A54
Chambers, J. E., Wetherill, G. W., & Boss, A. P. 1996, Icar, 119, 261
Collins, K. A., Kielkopf, J. F., Stassun, K. G., & Hessman, F. V. 2017, AJ, 153, 77
Dotter, A., Chaboyer, B., Jevremovic, D., et al. 2008, ApJS, 178, 89
Doyle, L. R., Carter, J. A., Fabrycky, D. C., et al. 2011, Sci, 333, 1602
Eastman, J., Siverd, R., & Gaudi, B. S. 2010, PASP, 122, 935
Endl, M., & Cochran, W. D. 2016, PASP, 128, 094502
Gaia Collaboration, Brown, A. G. A., Vallenari, A., et al. 2018, A&A, 616, A1
Gaia Collaboration, Prusti, T., de Bruijne, J. H. J., et al. 2016, A&A, 595, A1
Giménez, A. 2006, A&A, 450, 1231
Hairer, E., & Hairer, M. 2003, in Frontiers in Numerical Analysis (Durham, 2002), ed. J. Blowey, A. Craig, & T. Shardlow (Springer: Berlin), 199
Hilditch, R. W. 2001, An Introduction to Close Binary Stars (Cambridge: Cambridge Univ. Press)
Holman, M. J., & Wiegert, P. A. 1999, AJ, 117, 621
Hut, P. 1981, A&A, 99, 126
Kipping, D. M. 2013, MNRAS, 435, 2152
Kopparapu, R. K., Ramirez, R., Kasting, J. F., et al. 2013a, ApJ, 765, 131
Kopparapu, R. K., Ramirez, R., Kasting, J. F., et al. 2013b, ApJ, 770, 82
Kostov, V. B., McCullough, P. R., Carter, J. A., et al. 2014, ApJ, 784, 14
Kostov, V. B., Orosz, J. A., Welsh, W. F., et al. 2016, ApJ, 827, 86
Kratter, K. M., & Shannon, A. 2014, MNRAS, 437, 3727
Lam, C., & Kipping, D. 2018, MNRAS, 476, 5692
Li, G., Holman, M. J., & Tao, M. 2016, ApJ, 831, 96
Lissauer, J. J., Fabrycky, D. C., Ford, E. B., et al. 2011, Natur, 470, 53
Mandel, K., & Agol, E. 2002, ApJL, 580, L171
Mardling, R. A., & Lin, D. N. C. 2002, ApJ, 573, 829
Mazeh, T., Hoczer, T., Shporer, A., et al. 2015, ApJ, 800, 142
McQuillan, A., Aigrain, S., & Mazeh, T. 2013, MNRAS, 432, 1203
Mudryk, L. R., & Wu, Y. 2006, ApJ, 639, 423
Müller, T. W. A., & Haghighipour, N. 2014, ApJ, 782, 26
Orosz, J. A., & Hauschildt, P. H. 2000, A&A, 364, 265
Orosz, J. A., Welsh, W. F., Carter, J. A., et al. 2012, Sci, 337, 1511
Orosz, J. A., Welsh, W. F., Haghighipour, N., et al. 2019, AJ, 157, 174
Prša, A., Batalha, N., Slawson, R. W., et al. 2011, AJ, 141, 83
Quarles, B., Satyal, S., Kostov, V., et al. 2018, ApJ, 856, 150
Ragozzine, D., & Wolf, A. S. 2009, ApJ, 698, 1778
Rein, H., & Liu, S.-F. 2012, A&A, 537, A128
Rein, H., & Spiegel, D. S. 2015, MNRAS, 446, 1424
Riello, M., De Angeli, F., Evans, D. W., et al. 2018, A&A, 616, A3
Short, D. R., Orosz, J. A., Windmiller, G., et al. 2018, AJ, 156, 297
Skilling, J. 2004, in AIP Conf. Ser., Nested Sampling, ed. R. Fischer, R. Preuss, & U. V. Toussaint (Melville, NY: AIP), 395
Slawson, R. W., Prša, A., Welsh, W. F., et al. 2011, AJ, 142, 160S
Sutherland, A. P., & Kratter, K. M. 2019, MNRAS, 487, 3288
ter Braak, C. J. F., & Vrugt, J. A. 2006, S&C, 16, 239
Torres, G., Andersen, J., & Giménez, A. 2010, A&ARv, 18, 67
Tull, R. G. 1998, Proc. SPIE, 3355, 387
Tull, R. G., MacQueen, P. J., Sneden, C., & Lambert, D. L. 1995, PASP, 107, 251
Weiss, L. M., & Marcy, G. W. 2014, ApJL, 783, L6
Welsh, W. F., & Orosz, J. A. 2018, in Handbook of Exoplanets, ed. H. J. Deeg & J. A. Belmonte (Cham: Springer), 34
Welsh, W. F., Orosz, J. A., Carter, J. A., et al. 2012, Natur, 481, 475
Welsh, W. F., Orosz, J. A., Short, D. R., et al. 2015, ApJ, 809, 26
Wittenmyer, R. A., Welsh, W. F., Orosz, J. A., et al. 2005, ApJ, 632, 1157